Physics of the Earth and Planetary Interiors 350 (2024) 107160

Contents lists available at ScienceDirect

Physics of the Earth and Planetary Interiors

journal homepage: www.elsevier.com/locate/pepi

The onset of anelastic behavior in fine-grained synthetic dunite

Tongzhang Qu[a,c,*], Ian Jackson[a], Ulrich H. Faul[a,b], Emmanuel C. David[a,c]

[a] Research School of Earth Sciences, Australian National University, Acton ACT 0200, Australia
[b] Earth Atmospheric and Planetary Sciences, Massachusetts Institute of Technology, Cambridge, MA 02139, USA
[c] Department of Earth Sciences, University College London, London WC1E 6BS, UK

ARTICLE INFO

Keywords:
Improved forced-oscillation methods allow more precise examination of the onset of anelasticity in dry fine-grained dunite
A mild dissipation peak superimposed on monotonic background is newly and consistently observed at the onset of anelasticity
The newly observed dissipation peak is plausibly attributed to elastically accommodated grain-boundary sliding (EAGBS)
Water-mediated EAGBS in pure dunite is unable to explain seismological observations of the lithosphere-asthenosphere boundary

ABSTRACT

Micromechanical models suggest that the onset of anelastic relaxation in polycrystalline olivine, critical to interpretation of the seismic wave attenuation and dispersion in the upper mantle, should be a mild dissipation peak caused by elastically accommodated grain-boundary sliding. Such behavior has been tentatively invoked to explain both a short-period shear modulus deficit and a dissipation plateau poorly resolved at 900–700 °C in previous forced-oscillation experiments on fine-grained dunite tested within mild-steel jackets. However, these observations may have been complicated by the austenite to ferrite plus cementite phase transition in the jacket material, compliance associated with interfacial $Ni_{70}Fe_{30}$ foils, and modeling of the mechanical properties of polycrystalline alumina as control specimen. To investigate the influence of these complications within the experimental setup and provide forced-oscillation data of better quality especially at moderate temperatures, we have conducted further forced-oscillation tests for which we removed the interfacial foils, employed single-crystal sapphire as reference sample, and used alternative jacket materials (stainless steel or copper) which experience no phase transition during the staged cooling. The newly acquired forced-oscillation data, although broadly consistent with the previous results, differ significantly especially in temperature sensitivity, and allow refinement of an appropriate Burgers creep-function model. A mild dissipation peak superimposed on monotonic dissipation background during the onset of anelastic relaxation in dry, melt-free and fine-grained dunite has now been consistently observed at temperatures of ~950–1050 °C and seismic periods of 1–1000 s. Such a dissipation peak with relaxation strength 0.02 ± 0.01 is attributed to elastically accommodated grain-boundary sliding. The high activation energy (> 600 kJ/mol) of viscoelastic behavior involving both dissipation and related dispersion suggests that grain-boundary diffusion may be limited by interfacial reaction within grain boundaries. The reduced relaxation strength makes it difficult to attribute the oceanic lithosphere-asthenosphere boundary to water-mediated elastically accommodated grain-boundary sliding.

1. Introduction

High-temperature laboratory measurements of anelastic relaxation in dry and melt-free, fine-grained polycrystalline olivine have consistently shown essentially monotonic variation of strain-energy dissipation (Q^{-1}) associated with dispersion of shear modulus (G). The dissipation, dependent on period and described as ‘high-temperature background’ or ‘absorption band’, follows $Q^{-1} \propto T_o^{\alpha}$ where T_o is oscillation period $\alpha = 0.2$–0.4 (Anderson and Given, 1982; Karato and Spetzler, 1990; Jackson et al., 1992; Gribb and Cooper, 1998a). The laboratory measurement of such anelastic relaxation is crucial to interpret seismic velocity and attenuation structures (e.g. Wiens et al., 2006; Dalton and Faul, 2010; Ma et al., 2020; Havlin et al., 2021; Liu et al., 2023). Previous experimental studies demonstrated grain-size sensitivity of the anelastic relaxation (Tan et al., 2001; Jackson et al., 2002; Cooper, 2002, pp.14–17; Jackson and Faul, 2010), broad consistency between the activation energy of relaxation times and that of diffusional creep (e.g. Faul and Jackson, 2007), and the potential to parameterize the relaxation with a master variable that combines frequency, temperature, and grain size (McCarthy et al., 2011; Yamauchi and Takei, 2016). Accordingly, grain-boundary sliding (GBS) assisted or accommodated by diffusion has been invoked to explain the widely observed monotonic high-temperature background in attenuation spectrum and associated modulus dispersion.

The classic theory of GBS, developed by Raj and Ashby (1971) for a boundary of infinitesimal slope, was thoroughly reviewed by Jackson

---

* Corresponding author at: Department of Earth Sciences, University College London, London WC1E 6BS, UK.
E-mail address: tongzhang.qu@ucl.ac.uk (T. Qu).

https://doi.org/10.1016/j.pepi.2024.107160
Received 20 September 2023; Received in revised form 27 February 2024; Accepted 28 February 2024

et al. (2014) from which the following brief summary is extracted. At moderate temperature and/or relatively short duration of an applied stress, the strain incompatibility, resulting from a finite amount of slip in grain boundaries of relatively low viscosity, is accommodated by the elastic distortion of the participating grains. The strain associated with this process, called elastically accommodated grain-boundary sliding (EAGBS), is recoverable upon removal of the applied stress. Under a sinusoidally time-varying applied shear stress, the manifestation of such anelasticity is a dissipation peak (and associated modulus dispersion) with relaxation strength of order 10^{-1}, expected at a characteristic relaxation time following

$$\tau_e = \eta_{gb} d / G_U \delta \tag{1}$$

where δ and η_{gb} are the width and viscosity of the narrow grain boundary region, d is grain size, G_U is unrelaxed shear modulus.

The further analysis of GBS in the limit of infinitesimal grain-boundary slope by Morris and Jackson (2009) confirmed the general features of EAGBS proposed by Raj and Ashby (1971). However, subsequent studies suggest much lower relaxation strength of order 10^{-2} rather than 10^{-1} for sliding on boundaries of finite slope, with the dissipation peak reduced in height and broadened by any distribution of grain size and boundary viscosity (Lee and Morris, 2010; Lee et al., 2011). Thus, it is predicted that, with increasing temperature or oscillation period, the first significant indication of the breakdown of strictly elastic behavior in fine-grained materials should be a broad dissipation peak with amplitude of order 10^{-2} and associated modulus dispersion, reflecting anelastic relaxation behavior associated with EAGBS. At somewhat higher temperatures (T) and/or longer periods (T_o), a broad regime of diffusionally assisted grain-boundary sliding is predicted within which the dissipation varies with period as $Q^{-1} \propto T_o^{\alpha}$ with $\alpha \sim 1/3$, sliding being limited by stress concentrations at grain corners, that are progressively eroded with increasing period and diffusion distance. Ultimately, for periods longer than the Maxwell relaxation time $\tau_M = \eta_{ss}/G_U$ (η_{ss} is steady-state viscosity), diffusionally accommodated grain-boundary sliding occurs with $Q^{-1} \propto T_o$.

The sustained experimental campaign in our laboratory (e.g. Jackson and Faul, 2010; Jackson et al., 2014) and elsewhere (Gribb and Cooper, 1998a; Sundberg and Cooper, 2010; McCarthy et al., 2011; Takei et al., 2014) has so far revealed no more than circumstantial evidence of the dissipation peak expected of EAGBS in dry and melt-free olivine polycrystals or organic analogue material. For high-purity MgO, it has been suggested that the mild grain size sensitivity for the relaxation time τ_L, defining the well-resolved lower end of the anelastic absorption band, is consistent with the onset of EAGBS (Barnhoorn et al., 2016).

The difficulty of characterizing EAGBS by forced oscillation is perhaps not entirely surprising, as it is challenging to observe, superimposed upon the period-dependent background, the broad dissipation peak of low amplitude $\sim 10^{-2}$, predicted by the contemporary theoretical model (Lee and Morris, 2010; Lee et al., 2011). However, reconciliation of theory and experimental observations is critical for underpinning the robust extrapolation of experimental data for fine-grained geomaterials to the conditions of upper-mantle seismic wave propagation. That such conditions depart only modestly from ideal elastic behavior ($Q^{-1} < 0.03$, e.g. Romanowicz and Mitchell (2015)) places a special premium on the understanding of the transition from elastic to anelastic behavior, i.e. the onset of anelastic relaxation. Karato (2012) suggested that EAGBS influenced by water (hydrogen), might cause a large and sharp drop in seismic wave velocities at the lithosphere-asthenosphere boundary where water content likely changes (e.g., Karato et al., 1986; Hirth and Kohlstedt, 1996). Therefore, the goal of this work is to use improved experimental procedures and associated approaches of data processing to better test the hypothesis that the onset of anelastic relaxation in fine-grained, dry, melt-free dunite involves a dissipation peak associated with EAGBS.

For the purpose of minimizing uncertainty and therefore capturing the low dissipation and minor dispersion at the onset of anelastic relaxation in dunite, the experimental setup of our forced-oscillation testing has been updated. Almost all the previous work in our laboratory on dunite samples has been conducted within mild-steel jackets, lined for redox reasons by $Ni_{70}Fe_{30}$ (NiFe) foil. However, the correction required for the viscoelastic behavior of the enclosing mild-steel jacket is complicated by transformation of austenite, the high-temperature face-centred cubic (fcc) Fe—C phase, to ferrite (body-centered-cubic, bcc) + cementite (Fe_3C) during cooling from 900 to 700 °C (Jackson et al., 2000). Accordingly, we employed alternative jacket materials, including copper (restricted to temperatures ≤900 °C in Jackson et al. (2014) and extended to temperatures ≤1050 °C in this study, Appendix A) and austenitic stainless steel (≤ 1200 °C in this study), which remain fcc across the experimental temperature range. Other significant improvements of experimental methodology are described in Appendix B. In the following sections, we present observations of shear modulus dispersion and strain-energy dissipation during the onset of anelastic relaxation, a comparison of the new and previous observations, and a discussion of the correlation between the results and related theoretical studies.

2. Experimental materials and methods

2.1. Sample preparation

The synthetic dunite samples in this study were prepared from powders produced by solution-gelation method (Jackson et al., 2002). Magnesium nitrate ($Mg(NO_3)_2{\cdot}6H_2O$), ferric iron nitrate ($Fe(NO_3)_3{\cdot}9H_2O$)) and tetraethyl orthosilicate ($Si(OC_2H_5)_4$) were weighed in quantities sufficient for a 50-g batch containing 95 wt% forsterite (Fo_{90}) and 5 wt% enstatite (En_{90}) and dissolved in ethanol in an ultrasonic bath. The enstatite content buffers the silica activity in the samples. Once dissolution was complete, 2 mL nitric acid was added to initiate gelation with low heat then applied for 6 h. The resulting powder was pelletized and placed in a 1-atm furnace with 5/95 partial pressures of flowing CO/CO_2 at 875 °C ($\log(fO_2, \text{bar}) = -14.1$) for 16 h. Then the pellets were ground, re-pelletized, and placed in a 1-atm furnace with 50/50 partial pressures of CO/CO_2 at 1400 °C for 16 h ($\log(fO_2, \text{bar}) = -8.6$). After the firing, the pellets were ground in an agate ball mill until the polycrystalline aggregates of submicron grains were of dimension <50 μm, checked with optical microscope. Then the powder was pelletized again and fired again at 1400 °C with the 50/50 flowing CO/CO_2 gas mix for 16 h as above. This iterative process ensures complete dehydration and appropriate redox conditions for the porous gel-derived material.

For each specimen destined for mechanical testing, a stack of five 3-g cylindrical pellets of ~15-mm diameter and ~ 10-mm length, pre-fired as described above, was completely enclosed within $Ni_{70}Fe_{30}$ foil of 70 μm thickness. The wrapped stack of pellets was sandwiched between high-grade (Lucalox™) alumina pistons, jacketed by a mild-steel tube, and then hot-pressed for 24 h at 1200 °C and 300 MPa within an internally heated gas-charged pressure vessel (Paterson, 1970). After the hot pressing, the well-sintered and dense 5-pellet stack was extracted from the jacket and precision-ground into cylindrical shape. Then the hot-pressed specimens were fired at 600 °C in Ar for an hour to eliminate any water and lubricant introduced during grinding.

The specimens mechanically tested in runs A1464, A1802 and A1928 were newly prepared in this way. For details concerning the thermal histories of the various specimens, see Table 1. The specimen tested within a stainless-steel jacket in run A1802 was subsequently cut from the assembly and ground to remove the jacket, NiFe liner and the chemically modified outer rind of ~100-μm thickness. The ground sample was refired in controlled atmosphere with CO/CO_2 at 50/50 partial pressure at 1400 °C, and then assembled in the same way with alumina pistons and cylindrical NiFe liner but within a mild-steel jacket for follow-up forced-oscillation testing from 1300 °C in run A1906.

Table 1
Thermal history of experimental materials.

MT run number	HP temperature, °C [duration, hr]	Pre-firing temperature, °C [duration, h] (atmosphere)	MT temperature, °C
A1464	1200 [24]	600 [1] (Ar)	1050–25
A1802	1200 [24]	600 [1] (Ar)	1200–400† – 1200††
A1906	NA*	1400 [16] (50/50 CO/CO_2)	1300–900†
A1928	1200 [24]	600 [1] (Ar)	1300–400† – 1300††

MT: mechanical testing.
HP: isostatic hot pressing at 300 MPa.
* The sample of run A1906 was recycled from run A1802.
† Staged cooling (Section 2.3) to a minimum temperature at which a major gas leak intervened (900 °C) or oscillation of the experimental assembly was obstructed through contact with the pressure vessel (400 °C).
†† Highest testing temperature was revisited to check reproducibility of measurement.

2.2. Mechanical testing

The specimen was sandwiched directly between Lucalox™ alumina torsion rods within a thin-walled tube of either copper (Cu, run A1464), stainless steel (SS, run A1802) or mild steel (MS, runs A1906 and A1928) for mechanical testing in the apparatus described in detail by Jackson and Paterson (1993). For the tests within the MS and SS jackets (runs A1802, A1906 and A1928) from 1200 or 1300 °C, the cylindrical surface of the specimen was lined with NiFe foil for control of redox conditions (Faul et al., 2018), whereas the specimen was tested bare within the Cu jacket (run A1464) from 1050 °C.

The specimen assembly consisting of an olivine specimen, with or without a NiFe foil wrapper, alumina torsion rods and the metal jacket was loaded into the attenuation apparatus and pressurized initially to ~170 MPa within Ar medium at room temperature. The pressurization achieves firm direct frictional coupling between the specimen and the torsion rods, and a hollow steel member containing the elastic element within the apparatus. Following the raising of the specimen assembly to allow for thermal expansion and re-pressurization, the temperature was increased from 20 °C to the required maximum temperature (1300 °C for MS-jacketed assembly, 1200 °C for SS-jacketed assembly, and 1050 °C for Cu-jacketed assembly) at a rate of 6 °C/min, after which the pressure was adjusted to 200 MPa. The lower annealing temperature for the SS-jacketed assembly was intended to minimize diffusional communication between the stainless-steel jacket and the olivine specimen through NiFe liner, whereas that for the Cu-jacketed assembly was constrained by the melting point of copper (1084 °C). Before formal data acquisition, the forced-oscillation response was monitored during in-situ annealing

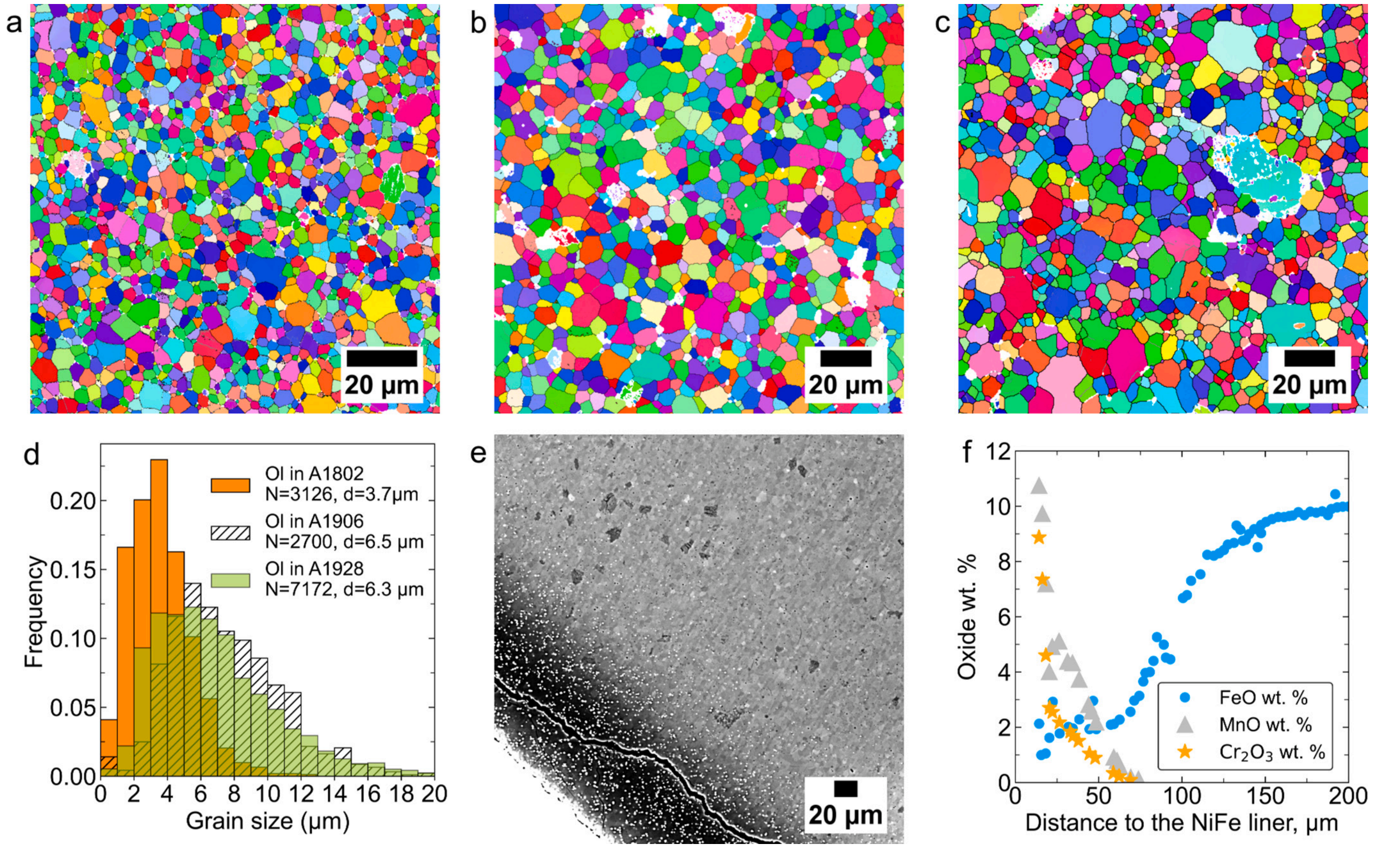

Fig. 1. (a)-(c) Inverse pole figure and grain boundaries based on EBSD data of samples after runs (a) A1802, (b) A1906, and (c) A1928. (d) The grain size distribution of olivine grains following testing in runs A1802, A1906 and A1928. N refers to the number of grains, and d is mean grain size. (e) Backscattered electron image of the sample and the NiFe liner (bright bottom-left corner) after run A1802. There is significant precipitation of Fe as blebs near the sample-liner interface, which formed a dark rind with ~100 μm width. The dark patches in light grey olivine of the interior are enstatite. (f) Quantitative EDS analysis of FeO, MnO and Cr_2O_3 from the sample-liner interface into the sample of run A1802. Analyses with FeO well above the surrounding points are deleted, since they partially reflect a contribution from metal blebs.

for over 20 h at peak temperature and 200 MPa. Such annealing stabilizes the specimen microstructure and frictional contacts between the specimen and the alumina torsion rods, considered responsible for modest temporal evolution of the mechanical behavior towards lower compliance and dissipation.

Torsional forced-oscillation testing at 200 MPa was conducted at temperatures ranging from the maximum temperature to room temperature by staged cooling with either 50 °C or 25 °C (for Cu-jacketed assembly) intervals. The cooling rate between the intervals for data collection was also 6 °C/min. A thermocouple (type R) was located within a hollow alumina piston, with its junction 3 mm above the top of the specimen. The furnace within the pressure vessel was calibrated, both before and after mechanical testing to ensure a flat temperature profile at the targeted temperature within ±10 °C along the length of the specimen. A sinusoidally time-varying torque was applied by a balanced pair of electromagnetic drivers at the lower end of experimental assembly comprising a series combination of the steel (elastic) element and the specimen assembly (c.f. Fig. 1a in Cline and Jackson, 2016). The distortions of the specimen assembly and elastic element were measured by two pairs of three-plate capacitance transducers. Each capacitance transducer consists of an outer pair of fixed plates and a central moving plate connected to the vertical axial member (including specimen assembly and attached elastic element) by a horizontal lever. With the completion of staged cooling to room temperature, the maximum temperature was usually briefly revisited to assess the reproducibility and check for strain-amplitude dependence of the results. At the revisited maximum temperature, we first ran a test with the same strain amplitude as during the staged cooling followed by a few more tests with smaller strain amplitudes. With the revisited testing finished, the temperature is reduced to room temperature at the rate of 6 °C/min.

Multiple stages of data processing are required to extract the low-frequency mechanical properties of olivine samples from the records of torsional displacements of specimen assembly and the elastic standard (Appendix B). Firstly, to eliminate the mechanical behavior of the steel and alumina torsion rods, the torsional compliance of the olivine specimen assembly was compared with that of a reference assembly containing a single-crystal sapphire control specimen. In the reference assembly, the sapphire specimen was similarly sandwiched between alumina torsion rods and alternatively jacketed by copper, SS or MS. Secondly, for each of the alternative jacket materials, corrections for the viscoelastic behavior of the metal jacket (inclusive of NiFe liner) were applied with forced-oscillation data acquired from prior tests on similarly jacketed cylindrical specimens of the metal materials (David and Jackson, 2018; Qu and Jackson, 2022). Details of data processing were described in Jackson and Paterson (1993).

The forced-oscillation data (G, $\log Q^{-1}$) of olivine specimens were fitted by a phenomenological rheology model based on extended Burgers-type creep function with different distributions of relaxation time for dissipation background and dissipation peak. A comprehensive description of the model has been recently provided (Qu et al., 2021).

Microcreep testing was practiced during the staged cooling from 1200 to 900 °C with 100 °C intervals, following the forced-oscillation testing at the same temperature. Constant rather than oscillating stress was applied for a prescribed duration in the testing. The proportions of the elastic, anelastic, and viscous components of transient creep are revealed at different temperatures, which provides complementary information in time domain. Before formal microcreep testing, any linear drift was estimated and corrected by a 2000-s session without any applied torque. Then torques of amplitude +L, 0, −L, 0 are successively applied to the specimen assembly, each for 2000 s duration. The multi-segment record $S_{\mathrm{rel}}(t) = S_{\mathrm{spc}}(t) - S_{\mathrm{ref}}(t)$, being the difference between the time-dependent torsional compliance of the olivine specimen assembly ($S_{\mathrm{spc}}(t)$) and that of reference assembly ($S_{\mathrm{ref}}(t)$), was modeled with an empirical Andrade-creep-function model $J(t) = J_{\mathrm{U}} + \beta t^{n} + t/\eta$. The measured differential microcreep record was fitted to a model $S_{\mathrm{fit}}(t)$ that is the sum of a suitably delayed contribution from each of the torque-switching events, i.e. $S_{\mathrm{fit}}(t) = \Sigma s_{\mathrm{i}} J(t - t_{\mathrm{i}})(\mathrm{i} = 1, 2, 3, 4)$ with $s_{\mathrm{i}} = 1$ when $\mathrm{i} = 1\ or\ 4$, and $s_{\mathrm{i}} = -1$ when $\mathrm{i} = 2\ or\ 3$, and $t - t_{\mathrm{i}}$ is the duration since the ith torque-switching event. The fitted creep model was converted to period domain and processed exactly as for forced-oscillation data (details in Jackson, 2019). The period-dependent torsional compliance of specimen thus finally inferred for the specimen $S_{\mathrm{mcp}}(T_0)$ fitted to an Andrade model, allows the construction of a virtual multi-segment microcreep record $S_{\mathrm{mcp}}(t)$ for the specimen itself. The associated maximum strain in the specimen (at its diameter) ($\varepsilon_{\mathrm{mcp}}(t)$) is calculated as $\varepsilon_{\mathrm{mcp}}(t) = S_{\mathrm{mcp}}(t)\varepsilon_{\mathrm{fo},Max}/S_{\mathrm{fo},Max}$ where $\varepsilon_{\mathrm{fo},Max}$ and $S_{\mathrm{fo},Max}$ are the maximum strain and torsional compliance during forced-oscillation testing.

2.3. *Microstructural characterization*

The microstructure of the specimen after each forced-oscillation experiment was assessed from the top of a disk sawn 1–2 mm from the upper sample-alumina contact. The disk was mounted in epoxy, polished with SiC (30 min), diamond paste (2 h), then alumina slurry (2–5 h), and finished with colloidal silica (50 min). The carbon-coated polished sections were imaged and analyzed by scanning electron microscopes (TESCAN VEGA3 and Hitachi 4300). The accelerating voltage of back-scattering electron (BSE) imaging is 15–25 kV. Energy dispersive X-ray spectroscopy (EDS) spot analyses were performed within the interior and near the edge of the olivine specimen. Electron backscattered diffraction (EBSD) mapping was processed by MTEX package. The step sizes for samples of runs A1802 and A1928 are 0.10 μm and 0.29 μm, respectively. High-angle grain boundaries were estimated when misorientation of neighboring pixels is >10°. The mean grain size is defined as 4/π times of the mean diameter of the area-equivalent circles for olivine grains.

3. Results

The results from sample characterization and mechanical tests of runs A1802 and A1928 with SS and MS jackets are presented in this section. Although the microstructure and forced-oscillation data of run A1906 with specimen recycled from A1802 have previously been described in Qu et al. (2021), these results are also displayed here to allow close comparison. For the specimen of run A1464, tested bare within a Cu jacket at temperatures reaching 1050 °C closely approaching the melting point of Cu (1084 °C), intense viscoelastic relaxation in Cu has the potential to mask the more subtle relaxation in olivine at such relatively low temperatures. Accordingly, details of this run, including forced-oscillation data, microstructural information and comparison with the results from SS-jacketed olivine, are presented in Appendix A and not further discussed in the main text.

3.1. *Microstructural and chemical analysis*

Microstructural and chemical information concerning the specimen tested within the SS jacket in run A1802 and that tested within the MS jackets of runs A1906 and A1928 are presented in Fig. 1. The EBSD maps in Fig. 1a-c for these three specimens show olivine grains of relatively uniform size arranged in ‘foam textures’ with mildly curved grain boundaries. The widely distributed accessory enstatite grains are not well resolved by EBSD, but given its small fraction, the grain size of pyroxene is not considered for estimation of mean grain size. The grain size distribution of olivine grains is summarized in Fig. 1d. The olivine grains in the interior of three samples are consistently composed of 40.9 ± 0.3 wt% SiO_2, 11.0 ± 0.2 wt% FeO and 48.4 ± 0.2 wt% MgO (Mg# = 88.7). Previous studies have shown little variation of olivine composition in the neighborhood of the enclosing $Ni_{70}Fe_{30}$ foil lined MS jacket – confirming chemical equilibrium with Fo_{90} olivine (Faul et al., 2018).

However, for run A1802 involving a $Ni_{70}Fe_{30}$ liner within an SS jacket, an outer dark rind of ~100-μm thickness is observed, wherein the olivine shows depletion in FeO (Fig. 1e). Close inspection of the liner-olivine interface found a thin pyroxene rind, < 10 μm wide, against the liner. Adjacent to the pyroxene rind, the original $Ni_{70}Fe_{30}$ liner now contains 46.3 wt% Fe, 40.4 wt% Ni, 9.6 wt% Cr, 0.3 wt% Mn. On the other side of the pyroxene rind, FeO in olivine is replaced by Cr_2O_3 and MnO. The enrichment of Cr_2O_3 and MnO in the olivine decreases to zero about 70 μm away from the interface shown in Fig. 1f. At this distance from the liner, olivine contains significantly more MgO and less FeO (over 55 wt% MgO vs 49.5% in the interior; FeO ~ 2 wt% vs 10 wt%), hence the low backscatter coefficient compared to the other area. Bright metal blebs widely distribute to ~200 μm into the sample. While the size of metal blebs is too small for precise analysis, they are found to be predominantly consisted of Fe with a small amount of Cr and Mn. Notably, there is no detectable Ni in the olivine or the metal blebs. The influence on redox conditions and potentially on mechanical measurements, imposed by the radially inward diffusion of Mn and Cr, is discussed in Section 4.2.

3.2. Mechanical testing results

The forced-oscillation data of the SS-jacketed and MS-jacketed dunite, acquired in runs A1802, A1906 and A1928, are displayed in Fig. 2. The three datasets share some common features. In general, as the temperature decreases, we observe increasingly weak period-dependence (dispersion) of shear modulus and less strain-energy dissipation. Between 1300 and 1150 °C, the slope of $\log Q^{-1}$ vs $\log T_o$ is slightly increased with longer periods, and between 1100 and 950 °C, this slope somewhat decreases at longer periods. For SS-jacketed olivine in run A1802, there is almost no detectable dissipation at temperatures below 900 °C, while for run 1928, the dissipation at and below 900 °C has been observed as scattered data independent of oscillation period T_o. All forced-oscillation data are tabulated in the supplementary material.

Almost identical strain-energy dissipation and modulus dispersion are obtained from the follow-up testing with the same strain amplitude after completion of staged cooling (1802120m versus 1802120o, and 1928130d versus 1928130i in Fig. 3). Revisit testing with various strain amplitudes at orders of 10^{-5}–10^{-6} also shows indistinguishable results. Such observations reflect solid reproducibility of the viscoelastic relaxation measurement and essential linearity of the stress-strain relation during the testing.

The results of microcreep testing are temperature dependent as demonstrated in Fig. 4. In the first 2000 s segment, the time-dependent inelastic component of strain is increased with higher temperature. At 1200 °C, the proportion of irrecoverable viscous component increased, especially in run A1802. At 1100 and 1000 °C, inelastic strain of the three testing is essentially recoverable within the second segment with torque removed and hence anelastic. The response to torque at 800–900 °C is nearly independent of time, and thus almost elastic for the three testing. The magnitude of anelastic strain among the three samples is similar.

4. Discussion

4.1. Statistical uncertainty and systematic error

As introduced in Section 2.2, the values of G and $\log Q^{-1}$ are derived from the raw experimental data through a multi-stage process involving comparison of the torsion compliances of the olivine specimen assembly and the single-crystal sapphire reference assembly, appropriate modeling of the elasticity of the sapphire control specimen, and of the viscoelastic behavior of the enclosing jacket inclusive of NiFe liner (details in Jackson and Paterson, 1993). The scatter among final data

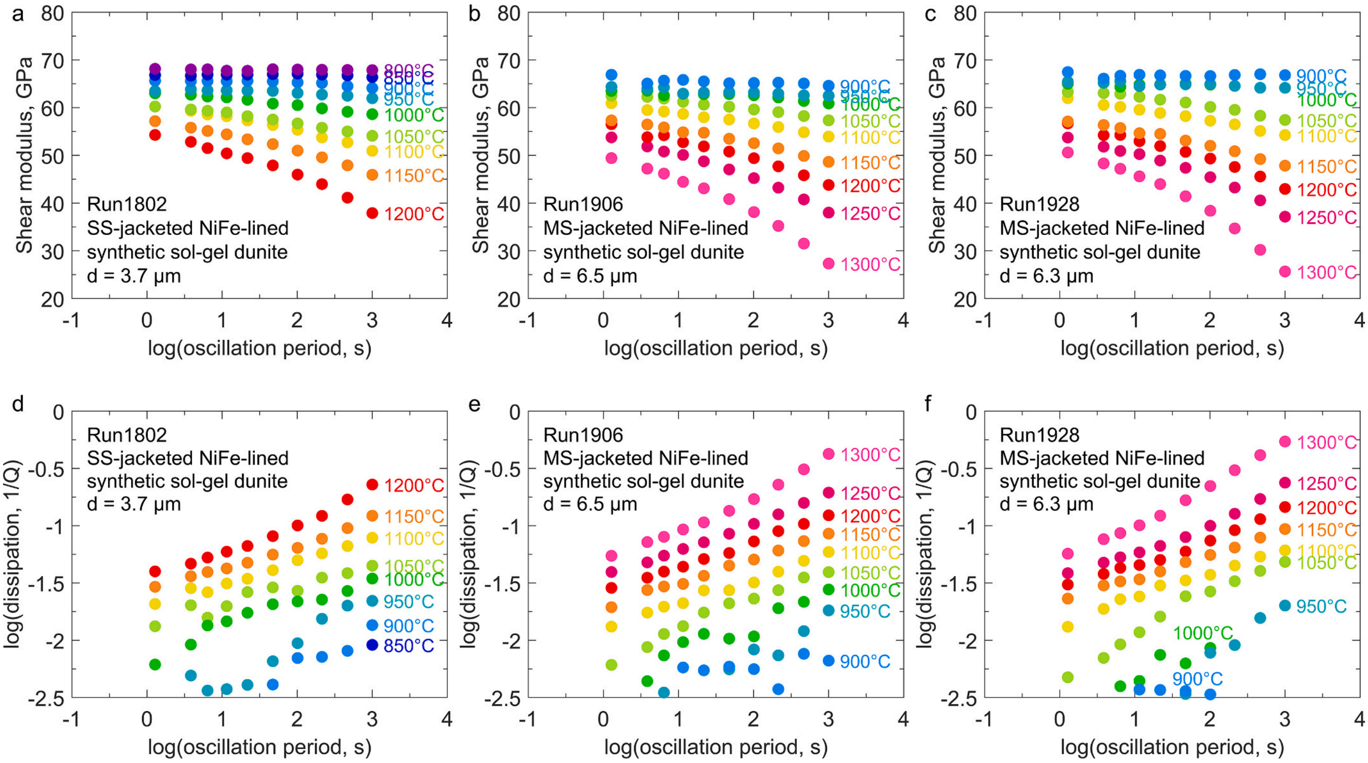

Fig. 2. Forced-oscillation data (G, $\log Q^{-1}$) newly obtained in this study for fine-grained synthetic dunite, alternatively contained within NiFe-lined SS and MS jackets. Temperatures are color coded. Mean grain size is referred as d in the subplots. The uncertainty of measurement is indicated approximately by the size of plotting symbols. (a) G and (d) $\log Q^{-1}$ for SS-jacketed dunite sample tested from 1200 to 800 °C in run A1802. (b) G and (e) $\log Q^{-1}$ for MS-jacketed dunite tested from 1300 to 900 °C in run A1906. (c) G and (f) $\log Q^{-1}$ of MS-jacketed olivine tested from 1300 °C to 900 °C in run A1928. The scatter amongst $\log Q^{-1}$ values ≤ -2.2 indicates the resolution limit of our mechanical testing.

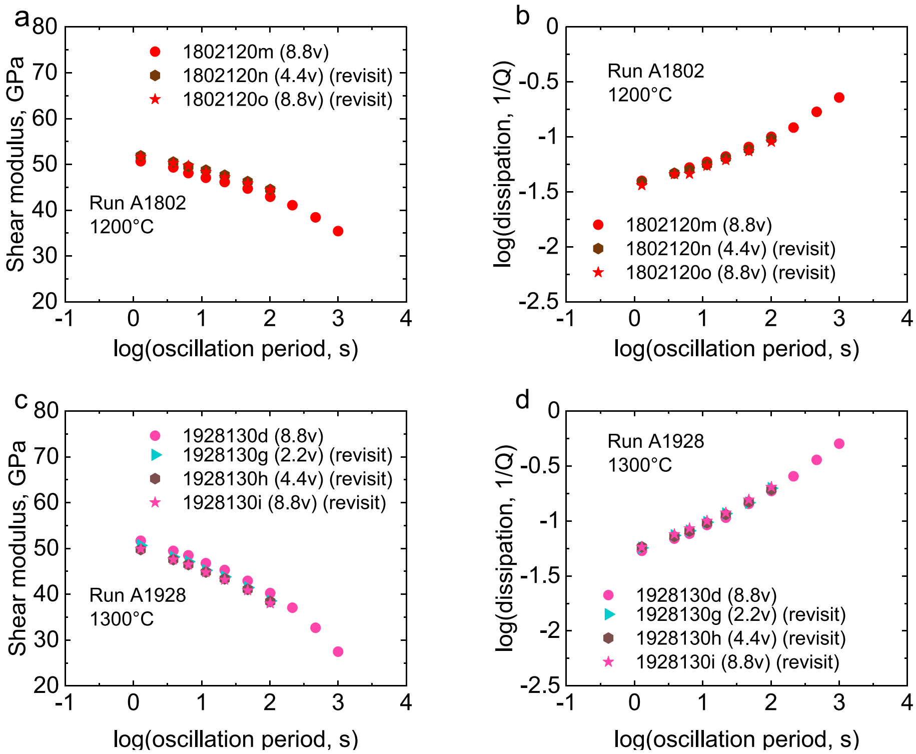

Fig. 3. Forced-oscillation data (G, $\log Q^{-1}$) from the testing before staged cooling (circles) and data from the revisited testing with various strain amplitudes. In the legends of subplots, the voltages following each run number (8.8, 4.4 and 2.2 V) are the voltages applied to the electromagnetic drivers. Corresponding strain amplitudes are 2×10^{-5}, 8×10^{-6} and 4×10^{-6} respectively. (a) G and (b) $\log Q^{-1}$ from run A1802 on SS-jacketed dunite. 1,802,120 m is the data at 1200 °C in Fig. 2a and d. (c) G and (d) $\log Q^{-1}$ from run A1928 on MS-jacketed dunite. 1928130d is the data at 1300 °C in Fig. 2c and f.

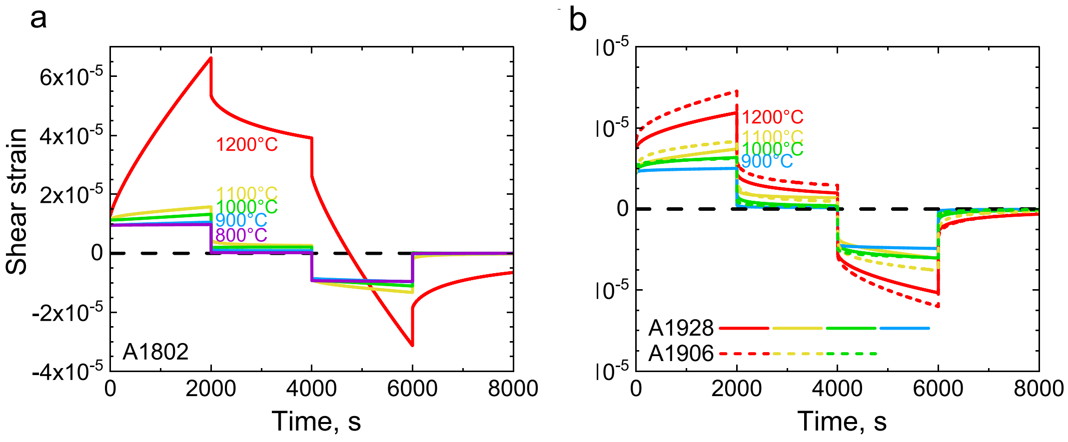

Fig. 4. Microcreep records for the olivine samples of runs A1802, A1906 and A1928, constructed by a multi-stage process involving comparison of microcreep records for specimen and reference assemblies and modeling of elastic/viscoelastic behavior of the sapphire control specimen and jacket material, respectively. Temperatures are color coded.

provides an indication of precision routinely quoted as $\sigma(G)/G = 0.03$ and $\sigma(\log Q^{-1}) = 0.05$. The appropriateness of these standard deviations is later confirmed by misfit values of χ^2 typically $\leq 2N$ for the optimal Burgers models fitted to N (G, Q^{-1}) data pairs for individual specimens. These standard deviations are to be regarded as average values across the entire range of testing conditions, although it is recognized that $\sigma(\log Q^{-1})$ increases significantly as $\log Q^{-1}$ decreases towards and beyond −2.

Observation of possible systematic error includes any mismatch of shear moduli at the maximum temperature before and after the staged cooling (Fig. 3a and c), and any inconsistency between the period-independent shear modulus measured by forced oscillation at medium to low temperatures and the unrelaxed shear modulus from high-frequency wave propagation methods (Isaak, 1992) illustrated in Fig. 5a and b. There are several possible sources of systematic error, besides the phase transition in mild-steel jacket (discussed in Section 4.2). Firstly, the pores and thermal cracking in the synthetic olivine aggregate could contribute to a modulus deficit, particularly at lower temperature (e.g., 400 °C in Fig. 5a). Secondly, any interfacial compliance between the specimen, control specimen, and the alumina and steel parts of the assemblies could contribute to a systematic offset (either positive or negative) between the low-frequency modulus and the high-frequency anharmonic trend as illustrated in Fig. 5a and b. Thirdly, any misalignment of the nominally parallel capacitance transducer plates

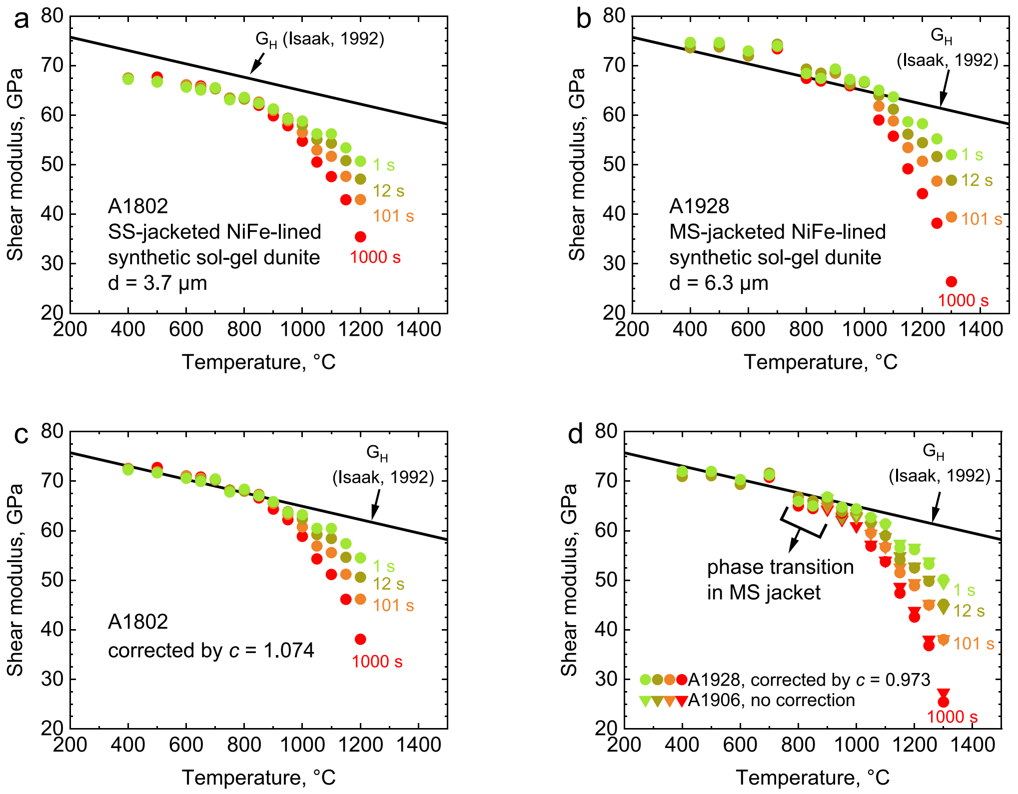

Fig. 5. The shear modulus measured in this study (markers) and compared with Hill average (G_H) of single-crystal elastic moduli for Fo_{90} (black line). Oscillation periods are color-coded. Shear modulus (a) of run A1802 and (b) of run A1928 before correction. Shear modulus (c) of run A1802 after correction by $c = 1.074$ for consistency of the 1 s modulus with the anharmonic trend at temperatures of 600–800 °C, and (d) run A1906 (triangles) and run A1928 after correction with $c = 0.973$ for consistency of the 1 s modulus with the anharmonic trend at temperatures of 400–1000 °C.

may result in systematic error in the measurement of displacements associated with the torsional distortion of the specimen and/or elastic standard and thereby have either positive or negative effect on the absolute value of shear modulus. These sources of systematic error will mainly affect the shear modulus, although any interfacial compliance between specimen/control specimen and adjacent alumina torsion rods might also contribute to the dissipation observed at high temperature.

A low-temperature modulus deficit consistently observed in the datasets of Jackson and Faul (2010), along with a poorly resolved dissipation plateau with Q^{-1}– 0.01 at 1–1000 s period and temperatures of 750–950 °C, was attributed to short-period anelastic relaxation, tentatively identified with elastically accommodated grain-boundary sliding. However, shear moduli subsequently measured in forced oscillation on olivine specimens at moderate-low temperatures have shown either negative or positive systematic deviations from the anharmonic trend (Fig. 2b in Farla et al., 2012; Cline, 2018, Ph.D. thesis). It has thus become apparent that the offset of shear modulus might not reflect the anelastic behavior of the sample, but instead be attributed to systematic errors in the experimental measurements.

Accordingly, and in order to focus attention on anelastic relaxation, we here take a different approach to the systematic offset between the high-frequency $G_H(T)$ trend and the period-independent (and hence elastic) modulus from forced-oscillation tests at low-moderate temperature. The multiplicative factor c that best accounts for the discrepancy in modulus is applied to scale all of the observed shear moduli G_{obs} in each of runs A1802 and A1928 in Fig. 2 to obtain scaled values of the modulus $G_{sc} = c \times G_{obs}$ that match the $G_H(T)$ trend ($c = 1.074$ for run A1802 and $c = 0.973$ for run A1928 in Fig. 5c and d). The modulus measured in run A1906 is not corrected (i.e., $c = 1.00$) due to the agreement between G_{obs} and $G_H(T)$ at 900 °C. After such scaling of moduli from run A1928, consistency between the moduli in runs A1906 and A1928 has been achieved (Fig. 5d).

4.2. Influence of updated experimental setup

Experimental procedures employed in our laboratory have evolved over many years and have recently been further refined, as explained in detail in Appendix B and summarized briefly here. The polycrystalline alumina control specimen has been replaced by a sapphire single-crystal control specimen. Also, the longstanding use of a NiFe foil at each end of the specimen and a double-foil at one end of the control specimen has been abandoned in favor of their direct contact with the torsion rods of Lucalox™ alumina. In Appendix B, we demonstrate almost absence of a substantial interfacial contribution to the compliance of the reference assembly involving such direct contact between the sapphire control specimen and alumina torsion rods. For the specimen assembly of the current methodology, chemical reaction between olivine specimen and alumina torsion rods in direct contact results in the formation of a refractory crystalline assemblage, amounting to a reaction bond, expected to be similarly of low compliance. Thus, uncertainties associated with interfacial compliance involving the NiFe foils and with the viscoelastic behavior of the polycrystalline alumina control specimen in the previous procedures of data processing have now been effectively eliminated.

Additionally, we have employed alternatives to the standard mild-steel (MS) jackets in which the occurrence of the austenite-to-ferrite phase transition during staged cooling might tend to obscure the onset of anelastic behavior in polycrystalline olivine. Cu jackets were employed by Jackson et al. (2014) and for run A1464 of this study (Appendix A), and an austenitic stainless steel (SS) jacket was used in run A1802 of this study. A NiFe liner wrapping the cylindrical surface of olivine sample within the SS-jacketed specimen assembly (as routinely used within MS jackets, e.g. Fig. 2a in Jackson et al. (2009)) is intended to chemically isolate the jacket material from the olivine sample and thereby maintain appropriate redox conditions for the stability of Fo_{90} olivine (Faul et al., 2018). However, the Mn and Cr from the SS jacket in run 1802 have evidently diffused through the NiFe liner, displacing much of the Fe from olivine in the outermost part of the specimen. Cr-Cr$_2$O$_3$ buffer was measured to be 5 log(fO2, bar) unit below iron-wüstite (Holzheid and O'Neill, 1995), and the free energy of Mn-MnO buffer is even lower than Cr-Cr$_2$O$_3$ buffer (Alcock and Zador, 1967). Although the activities of Cr and Mn in the alloy liner are obviously much less than unity, the coexistence of the pyroxene rind next to the sample-liner interface along with Fe-rich metal blebs is indicative of the decomposition of fayalite according to the reaction $Fe_2SiO_4 = FeSiO_3 + Fe + (1/2)O_2$ suggesting redox condition below the olivine-pyroxene-iron (OPI) equilibrium (see Nitsan (1974) for complete presentation of the fO$_2$-T diagram of the system). From the pyroxene rind up to 200 μm into the sample, the FeO content in olivine progressively increases from 2 to 10 wt%, along with the presence of pervasive metal blebs, reflecting gradual increase in fO$_2$ near OPI equilibrium. The main body of the sample, without any metal blebs, therefore maintained redox states above OPI equilibrium during run A1802. Analyses on similar sol-gel dunite samples have shown that the fO$_2$ change had propagated substantially further into the sample than the compositional changes at the liner-sample interface (Faul et al., 2018). Accordingly, the fO$_2$ in the SS-jacketed sample is lower than the fO$_2$ in MS-jacketed samples throughout.

To provide more data with modern experimental setup, this tested SS-jacketed sol-gel olivine specimen (run A1802, annealed at 1200 °C, final grain size 3.7 μm) was cut from the assembly and ground to remove stainless-steel jacket, NiFe liner and the most chemically modified outer rind of ~100-μm thickness. The ground sample was refired in controlled atmosphere with CO/CO$_2$ at 50/50 partial pressure at 1400 °C, and then assembled in the same way with alumina pistons and cylindrical NiFe liner but within an MS jacket for follow-up forced-oscillation testing from 1300 °C in run A1906. For further comparison, another, newly hot-pressed, olivine sample was tested in a mild-steel jacket from 1300 °C (run A1928). Because the mild-steel jacketed olivine samples were fired/annealed at higher temperatures than 1200 °C before staged cooling, these specimens are significantly more coarse-grained than that from run A1802 (Table 2).

The forced-oscillation data for the specimens, tested in runs A1802, A1906 and A1928, have already been presented in Fig. 2 of this study and Fig. 4a and b in Qu et al. (2021) as variations of G and logQ^{-1} vs logT_o at each of a series of fixed temperatures. However, a clearer overview might be available from an alternative presentation, as follows. Where the mechanisms responsible for the dissipation background and any superimposed peak are thermally activated with a common activation energy, the strain-energy dissipation log(Q^{-1}) and modulus relaxation ($G - G_U(T)$) may be expressed as a function of a pseudoperiod (X) master variable (Kê, 1947; Jackson et al., 2002), defined by

$$X = T_o exp\left[\left(-\frac{E}{\mathrm{R}}\right)\left(\frac{1}{T}-\frac{1}{T_\mathrm{R}}\right)\right] \tag{2}$$

where E is activation energy, regular R is gas constant, T is temperature, and subscript R refers to reference temperature at 1173 K. The variable X is appropriately termed a pseudoperiod as $X = T_o$ for $T = T_R$. Under these circumstances, the modulus relaxation and dissipation may be expected to collapse onto separate master curves for each sample. This approach has the potential to enhance the coherence amongst the data and suppress the influence of scatter especially at low levels of dissipation. In order to evaluate multiple influences on the mechanical behavior potentially from assembly setup, forced-oscillation data of reference assembly, and jacket material, chemical composition (or redox conditions) and annealing temperature (or grain size), several instructive comparisons are presented in Fig. 6 as follows:

Table 2
The optimal Burgers models[a].

Specimen	SS-jacketed dunite	MS-jacketed dunite	MS-jacketed dunite
Run number	A1802	A1906	A1928
Temperature, °C	900[b] – 1200	900[c] – 1300	1050[d] – 1300
logQ^{-1}_{min}	−2.3[b]	−2.3[c]	−2.3[d]
N, number of (G, Q^{-1}) data pairs	59	75	59
d, average grain size (μm)	3.7	6.5	6.3
Pressure (GPa)	0.2	0.2	0.2
T_R, reference temperature (K)	1173	1173	1173
G_{UR}, unrelaxed shear modulus at reference temperature (GPa)	[66.5]	[66.5]	[66.5]
dG_U/dT, (GPa K^{-1})	[−0.0136]	[−0.0136]	[−0.0136]
Δ_B, relaxation strength of dissipation background	0.76(4)	0.93(3)	0.87(3)
α, frequency dependence of background relaxation time distribution	0.217(7)	0.222 (5)	0.250(7)
log(τ_{LR}, s), lower bound of background relaxation time distribution	[−4.0]	[−4.0]	[−5.0]
log(τ_{HR}) = log(τ_{MR}, s), upper bound of background relaxation time distribution	8.87(17)	9.93(15)	9.68(18)
Δ_P, relaxation strength of dissipation peak	0.012(3)	0.006(3)	0.029(4)
log(τ_{PR}, s), logarithm of the center of peak relaxation time distribution at reference temperature	3.7(2)	4.8(3)	5.1(1)
σ, width of dissipation peak	[1.1]	[0.6]	[0.9]
E_B, activation energy of dissipation background (kJ/ mol)	660(18)	671(13)	664(16)
E_P, activation energy of dissipation peak (kJ/ mol)	[660]	[671]	[664]
χ^2_G	18.5	36.3	35.6
$\chi^2_{1/Q}$	56.5	80.3	59.5
χ^2_T, total misfit	74.9	116.6	95.2
$(\chi^2_T/2\ N)^{1/2}$	0.80	0.88	0.90

[a] Values followed by a value in parentheses are refined during the non-linear least-squares fitting, whereas values in square brackets are instead manually adjusted to achieve the smallest fit. The numbers in parentheses are the uncertainties applied to the last digit of the refined values. The parameter uncertainties are formal one-σ values, reflecting the scatter of data about the best fitting model, i.e. the precision rather than absolute accuracy of data.

[b] Exclusion of long-period data at 950 and 900 °C reduces the average misfit from 0.80 to 0.66 without significantly perturbing the preferred model; inclusion of an additional (G, Q^{-1}) pair with log$Q^{-1} > -2.3$ at 850 °C and 1000 s has minimal impact upon the model but increases $(\chi^2/2\ N)^{1/2}$ somewhat to 0.86.

[c] Exclusion of 7 long-period data at 950 and 900 °C reduces $(\chi^2/2\ N)^{1/2}$ from 0.88 of the preferred model to 0.83.

[d] Inclusion of 7 additional (G, Q^{-1}) data pairs with log $Q^{-1} > -2.3$ at 1000 and 950 °C markedly increases the average misfit to 1.12 without significantly perturbing the preferred model.

(i) Forced-oscillation data, acquired with the new methodology, for SS-jacketed fine-grained olivine (d = 3.7 μm of run A1802) are compared with a Burgers 'background + peak' model fitted to forced-oscillation data obtained with the superseded methodology for the mild-steel jacketed sample of run A1127 (sol-gel olivine, d ~ 3.6 μm, recently reprocessed from Jackson and Faul, 2010) in Fig. 6a and b. Although there is a broad qualitative consistency between the two datasets, the data from run A1802 reveal milder dispersion and lower dissipation than for specimen A1127, but with stronger temperature dependence.

(ii) Forced-oscillation data for the relatively coarse-grained recycled specimen of run A1906 and the specimen newly prepared for A1928 (with d ~ 6.5 and 6.3 μm, respectively) are closely consistent in Fig. 6c and d.

(iii) The pseudoperiod approach has been applied to the datasets (A1802, A1906, A1928) obtained with the modern experimental methodology with estimated E = 660 kJ/mol, and to the data obtained with the old experimental setup (A1127 of Jackson and

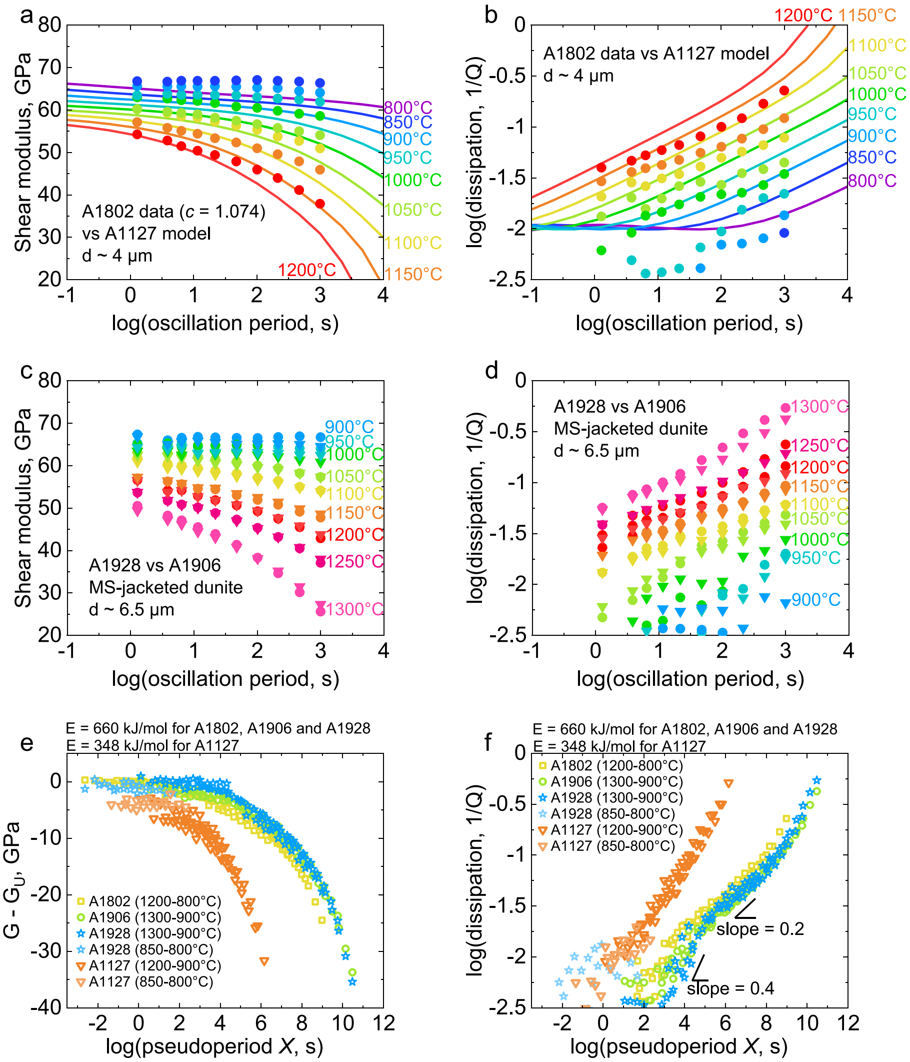

Fig. 6. Comparison between forced-oscillation data and models, including run A1127: fine-grained olivine samples tested with old experimental setup (MS-jacketed, annealed at 1200 °C) (Jackson and Faul, 2010); A1802: fine-grained olivine sample tested with modern setup (SS-jacketed, annealed at 1200 °C); A1906: recycled A1802 tested with modern setup (MS-jacketed, annealed at 1300 °C); A1928: olivine sample tested with modern setup (MS-jacketed, annealed at 1300 °C). (a)(b) Forced-oscillation data of A1802 (markers) vs Burgers model of A1127 (solid lines). (c)(d) Forced-oscillation data of A1928 (circles) and A1906 (triangles). (e)(f) Modulus relaxation ($G - G_U(T)$) and dissipation (Q^{-1}) plotted against pseudoperiod with estimated activation energy. Dissipation data from run A1802 at $X < -2$ are mostly below −2.5 in log scale and therefore not shown in subplot f. Light blue and orange symbols present data at 850–800 °C potentially complicated by fcc-bcc transition in MS jackets.

Faul (2010) recently reprocessed) with much lower apparent $E =$ 348 kJ/mol in Fig. 6e and f. The data for runs A1906 and A1928 define common $[G - G_U(T)](X)$ and $\log Q^{-1}(X)$ master curves, emphasizing their consistency. The somewhat stronger modulus dispersion and dissipation for the specimen of run A1802 are probably attributable mainly to its smaller grain size. The range of the pseudoperiod variable X defines the range of oscillation periods at the reference temperature T_R (900 °C) that would be equivalent mechanically to the actual testing periods at the generally higher, but also lower, temperatures. For example, for the specimen of run A1928, the testing at oscillation periods of 1–1000 s and temperatures of 800–1300 °C, spans the range $-2 < \log X < 10.5$ – equivalent to oscillation periods at 900 °C of 0.01 s to 1000 y evidently encompassing much of the entire relaxation spectrum (Fig. 6e and f). With the much lower activation energy for run A1127, similar ranges of dispersion and dissipation are associated with a much narrower range of $\log X$.

Observation (i) suggests that significant mechanical influence results from the updates in experimental setup including the removal of interfacial NiFe liners and replacement of polycrystalline alumina reference sample by sapphire (Appendix B). The similar results in (ii) obtained on the fresh and recycled specimens of runs A1928 and A1906 suggest that the recycled and refired specimen A1906 bore no legacy of its prior testing under more reducing conditions within SS jacket of run A1802. Allowing for the influence of grain size variation, the consistency of the data from runs A1802, A1906 and A1928 (observation (iii)) demonstrates that our procedures for data processing have successfully characterized the viscoelastic behavior of the alternative SS and MS jacket materials, and mostly erased the influence of the jacket from the final forced-oscillation data. Also, there can be no major influence of the somewhat more reducing conditions within the NiFe-lined SS jacket of run A1802.

The dissipation ‘plateau’, tentatively identified by Jackson and Faul (2010) at the lowest measurable levels of dissipation ($\log Q^{-1} \sim -2$) and moderate temperatures (850–700 °C) is evident in the dissipation data for MS-jacketed olivine - for run A1127 in Fig. 6b (light orange symbols) and for run A1928 in Fig. 6f (light blue symbols), with some impact on the shear modulus for run 1928 in Fig. 5d. This feature in both modulus and dissipation is conspicuously absent from the data for the SS-jacketed sample of run A1802 (Fig. 2a and b and Fig. 6f), which shows instead monotonic variation of modulus dispersion with temperature and only a subtle variation of slope of the $\log Q^{-1}$ vs $\log T_o$ trends at 950–1050 °C that is more clearly evident in the pseudoperiod plot. This contrast and the scattering of dissipation data <900 °C for runs A1127 and A1928 in light color in Fig. 6f suggest that the microstructures and mechanical properties of MS jackets – known to be sensitive to thermal history including cooling rates and dwell times and therefore not very reproducible – complicate the removal of the influence of the jacket from the mechanical behavior inferred for the olivine specimen. However, such complications in the mechanical behavior of the MS jacket do not in fact mask the onset at 950–1050 °C of substantially anelastic behavior observed with the improved experimental methods.

4.3. Onset of anelastic relaxation in dry and melt-free fine-grained dunite

The modulus and dissipation data, obtained with the new methodology for forced-oscillation testing, indicate the onset of observable anelastic relaxation ($\log Q^{-1} > -2.2$) in fine-grained olivine aggregates at temperatures of 950–1050 °C. This temperature range is consistent with the onset of appreciably anelastic response in microcreep testing in Fig. 4 and the onset of modulus dispersion in Fig. 5. Subtle variation of the slopes of the $\log Q^{-1}$ vs $\log T_o$ trends at these moderate temperatures demonstrated in Fig. 2 suggests the presence of a dissipation peak of modest amplitude superimposed upon the monotonic background, that is most clearly revealed by the strong variation of the slope of the $\log Q^{-1} - \log X$ trend at $\log X \sim 3$–5 in Fig. 6f. At the same range of $\log X$ in Fig. 6e, modulus relaxation becomes detectable. Such evidence of a dissipation peak is present in the data from each of the runs A1802, A1906 and A1928, but at best marginal for run A1127 with the superseded methodology.

In order to further assess such evidence for a dissipation peak superimposed upon the background relaxation, the forced-oscillation data were fitted to alternative models based on creep functions of the extended Burgers type (details in Qu et al., 2021; nomenclature and values of parameters in Table 2). For this purpose, (G, Q^{-1}) data pairs with $\log Q^{-1} < -2.3$ have been excluded along with some additional scattered/outlying data at relatively low temperatures, as noted in Table 2 and plotted as open circles in Fig. 7. Initially, the remaining N (G, Q^{-1}) data pairs were fitted to a background-only model. Subsequently, separate distributions of relaxation time were included to account for the dissipation background and superimposed peak, along with the corresponding modulus dispersion. Inclusion of the additional peak-related relaxation was found to reduce the total variance $\chi^2_T = \chi^2_G + \chi^2_{1/Q}$ markedly for runs A1802 and A1928 by 17 and 30% respectively, thereby providing additional support its existence. For A1906, the corresponding 5% reduction in variance is more marginal. The evidence from Fig. 6e and f, that a single activation energy is sufficient to achieve a reasonable master curve for the relaxation spectrum including dissipation peak and background (and related modulus relaxation) is supported by the fact that the 'background + peak' models of Table 2 do not (statistically) require an activation energy for the peak relaxation distinct from that of the background. The value of $(\chi^2_T/2\,N)^{1/2} < 1$ for each of the fitted datasets indicates that on average the G and $\log Q^{-1}$ data are fitted within one standard deviation ($\sigma(G)/G = 0.03$ and $\sigma(\log Q^{-1}) = 0.05$, respectively). The unrelaxed shear modulus G_U and its temperature dependence are fixed at anharmonic values (Isaak, 1992), and the other parameters concerning the distributions of background and peak relaxation times are in general consistency among the fits for the three datasets.

The models presented in Table 2 differ significantly from those of previous studies. The parameter $\alpha \approx \partial \log Q^{-1}/\partial \log T_o$ is consistently somewhat lower at 0.233 ± 0.023 compared to 0.274 ± 0.005 found in previous research (Jackson and Faul, 2010). Similarly, the activation energy E, describing the temperature dependence of the relaxation times, displays systematically higher values (662 ± 20 kJ/mol) compared to the ~400 kJ/mol reported by Jackson and Faul (2010). Previously reported dissipation peak characteristics with $\Delta_P = 0.057 \pm 0.002$, $\sigma = 4$ and $\log(\tau_{PR}, s) = -3.4 \pm 0.1$ (from the optimal fit of previous forced-oscillation dataset from five essentially melt-free samples from Jackson and Faul (2010)) contrast with those newly constrained $\Delta_P = 0.018 \pm 0.015$, $\sigma = 0.85 \pm 0.25$ and $\log(\tau_{PR}, s) = 4.35 \pm 0.85$ by averaging over the three specimens of Table 2. Because the parameters for the dissipation peak are constrained by only modest additional dissipation relative to the background, they range more widely among the three models than suggested by their formal 1σ uncertainties. Nevertheless, it is clear that these newly constrained features of dissipation peak differ substantially from the results of our previous studies.

The activation energy for each experiment, now constrained by the fitting, has been separately applied to the pseudoperiod plots of fitted data and Burgers model in Fig. 8, further demonstrating the existence of dissipation peak with the same activation energy as dissipation background. The previously identified peak, e.g. as illustrated by run A1127 in Fig. 8, reflects instead the scattered dissipation data and mismatch between measured shear modulus and unrelaxed shear modulus at temperatures below 900 °C, now regarded as a complication caused by phase transition in mild-steel jacket as discussed in Section 4.2.

4.4. Elastically accommodated grain-boundary sliding

Elastically accommodated grain-boundary sliding (EAGBS) has been described as the relative displacement parallel with the boundary of adjacent grains facilitated by low effective viscosity of grain boundary. This sliding on non-planar grain boundaries lead to a back stress from distorted grains via Hooke's law inhibiting further slip. Spatially, the back stress is distributed along the grain boundaries and concentrated at curvature along grain boundaries, e.g., at grain corners. Temporarily, the back stress concentration grows as sliding continues and ultimately balances the applied shear stress. The development of back stress demonstrates that EAGBS is a process of transient creep with anelastic strain to accommodate to the incompatibility among grains (Raj and Ashby, 1971). In frequency domain, a dissipation peak is anticipated by EAGBS model at relatively low homologous temperature (Zener, 1952; Morris and Jackson, 2009; Lee and Morris, 2010) and experimentally observed in metallic materials (e.g. Kê, 1947). Yet most of the mechanical loss peaks observed in previous studies of polycrystalline olivine are associated with presence of melt (Jackson et al., 2004; Xu et al., 2004) or premelting effects reported for organic rock analogue material at high homologous temperature (Yamauchi and Takei, 2016). Observations of a high-temperature peak (1250–1300 °C) in an olivine-pyroxene mixture were attributed to EAGBS by Sundberg and Cooper (2010), but may instead reflect the presence of melt in their samples derived from natural precursor (Qu et al., 2021). The dissipation plateau in Jackson and Faul (2010) was modeled as part of a short-period dissipation peak centered beyond the observational window (Figs. 6b and 8) to account for short-period deficit (now sidelined by scaling strategy in Section 4.1), tentatively attributed to EAGBS. However, as discussed in Section 4.2, if such a dissipation plateau were mechanical loss in olivine, it should be evident in the data for SS-jacketed olivine from the present study with the new methodology (run A1802) – from which it is absent.

The results of this study with both SS and MS jackets thus provide the first clear experimental observation of a mild dissipation peak superimposed upon background for genuinely melt-free and dry dunite samples. Such a dissipation peak is consistent with the theory of EAGBS in several respects. Firstly, the microcreep records suggest that the peak lies within the temperature range of mildly anelastic behavior (Fig. 4). Secondly, the onset of modulus relaxation occurs at $4 < X < 5$ in Fig. 6e, consistent with the pseudoperiod of dissipation peak in Fig. 6f. Thirdly,

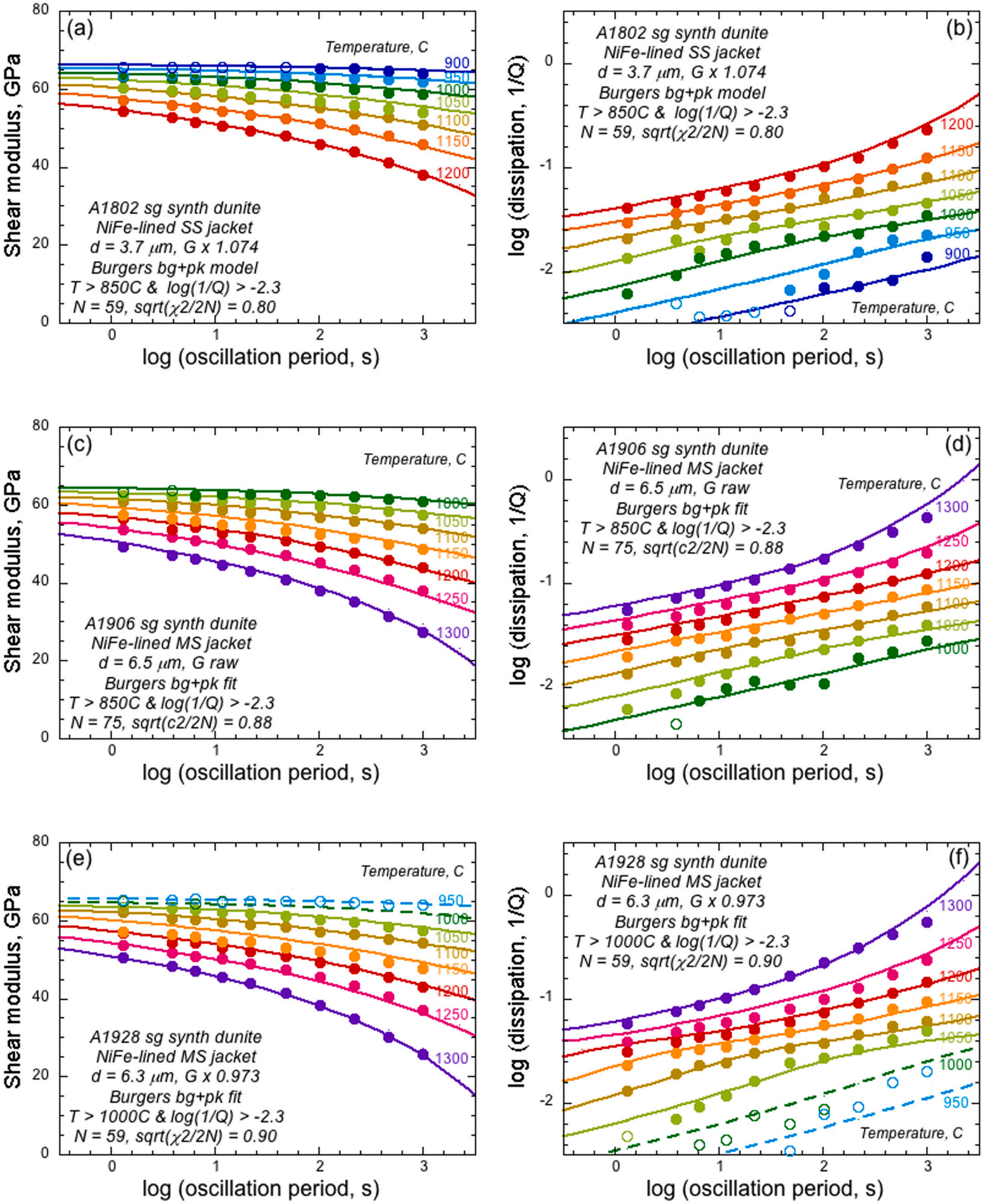

Fig. 7. Extended Burgers model fitted to the forced-oscillation data of A1802, A1906 and A1928. Modulus data in a and e have been scaled as in Section 4.1. Forced-oscillation data excluded from the fitted dataset are plotted as hollow markers, and the fit unconstrained by any data at the corresponding temperature is plotted in broken lines.

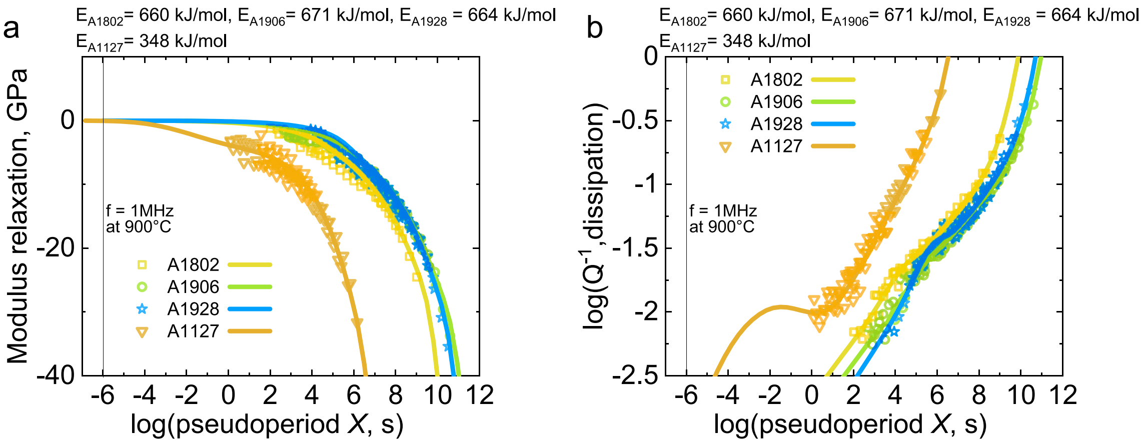

Fig. 8. Forced-oscillation data and fitted Burgers model plotted against log$X$. Only data used for fitting were plotted.

the modest relaxation strength (~0.01–0.03) is consistent with the outcome of micromechanical modeling, specifically the finding that finite boundary slope and variations of grain size or grain-boundary viscosity result in a predicted relaxation strength of order 10^{-2} for EAGBS (Lee and Morris, 2010; Lee et al., 2011; Jackson et al., 2014).

The micromechanical model which guides our thinking about grain-boundary sliding invokes an effective viscosity for elastically accommodated sliding on the boundary, with either a unique representative value or a distribution. This seems to be appropriate for the very wide range of atomic-scale grain-boundary structures, with or without impurity segregations, that must be present in a polycrystal of randomly oriented grains. Others have sought to describe the structure and behavior of grain boundaries in terms of the presence of specific grain-boundary defects termed disconnections (either dislocations or disclinations) (Cordier et al., 2014; Hirth et al., 2019; Hirth et al., 2020) or complexions (distinct grain-boundary ‘phases’) (e.g. Cantwell et al., 2014). However, microstructural evidence of such features is limited. In particular, high-resolution TEM (HRTEM) images of general, high-angle grain boundaries show abutting lattice planes of adjacent crystals (Vaughan et al., 1982; Hiraga et al., 2002; Marquardt and Faul, 2018); or neighboring crystals separated by a disordered region with about 1 nm or less in width (Drury and Fitz Gerald, 1996; Tan et al., 2001; Faul et al., 2004). The TEM images show no ubiquitous interfacial or linear defects that are common to all grain boundaries. As grain boundary orientations in a polycrystal without preferred orientation are random (e.g. Faul & Fitz Gerald (1999, and references therein)), it is reasonable to model the grain-boundary viscosity with a representative value or distribution.

With the dissipation peak attributed to elastically accommodated grain-boundary sliding, Eq. (1) can be used to estimate the grain-boundary viscosity η_{gb} as

$$\eta_{gb} = G_U(T)\delta\tau_P(T)/d = G_U(T)\delta\tau_{PR} exp[(E_P/R)(1/T - 1/T_R)]/d \tag{3}$$

with grain-boundary width $\delta \sim 1$ nm (Faul et al., 2004) and values for T_R, d, G_U, τ_{PR} and E_P from Table 2. The η_{gb} thus calculated from $\tau_P(T)$ is compared with the η_{gb} calculated by theoretical models and other experimental measurements.

Assuming that grain boundaries are perfect sinks for vacancies, Ashby (1972) proposed the lower limit of grain-boundary viscosity as

$$\eta_{gb} = \frac{kT}{8bD_{gb}} \tag{4}$$

where k is Boltzmann constant, b is atom size, and D_{gb} is the grain-boundary diffusivity with temperature dependence given by

$$D_{gb} = \frac{A_{gb}}{\delta} exp\left(-\frac{E_{gb}}{RT}\right) \tag{5}$$

For boundary diffusion of the slowest-diffusing Si in dry and melt-free forsterite, the pre-exponential factor A_{gb} and activation energy E_{gb} were found to $10^{-16.3\pm1.2}$ m^3/s and 220 ± 30 kJ/mol (Fei et al., 2016). Here the pressure dependence of D_{gb} is ignored because the relevant activation volume has not been well constrained, and the experimental pressure of forced-oscillation testing is only 200 MPa. Alternatively, D_{gb} can be estimated from the steady-state viscosity η_{SS} for (Coble) diffusional creep through the expression

$$D_{gb} = \frac{kTd^3}{132\delta\eta_{SS}\Omega} \tag{6}$$

(Raj and Ashby, 1971) where υ, d, Ω are Poisson’s ratio, grain size and molecular volume of the diffusing species. The steady-state viscosity η_C in compressive diffusional creep in sol-gel olivine was calculated as stress (σ_1) divided by strain rate ($\dot{\varepsilon}_1$) from Fig. 14 in Faul and Jackson (2007), subsequently converted to η_{SS} for pure shear following Eq. (1.5) in Frost and Ashby (1982) (i.e. $\eta_{SS} = \frac{\sigma_{shear}}{\dot{\varepsilon}_{shear}} = \frac{\sigma_1/\sqrt{3}}{\sqrt{3}\dot{\varepsilon}_1} = \eta_C/3$) (see also Jackson, 2000). Then we applied Eq. (6) to the diffusional creep rheology for sol-gel olivine with $d = 5$ μm, and $\Omega = 2.9 \times 10^{-28}$ m^3 (Fujino et al., 1981) to infer values of D_{gb} and thus η_{gb} (via Eq. (4)).

Grain-boundary viscosities thus estimated from τ_P, grain-boundary diffusivity, or diffusional creep are compared with a direct measurement of grain-boundary viscosity of iron-free bicrystal from Thom et al. (2020) in Fig. 9. Although grain-boundary diffusivities and therefore the grain-boundary sliding rates are influenced by iron content, the creep rates of iron-bearing olivine in Yabe et al. (2020) agree well with those of iron-free forsterite from Nakakoji et al. (2018) in diffusional creep regime (Fig. 14 in Yabe et al., 2020). We find similar broad compatibility in Fig. 9 between grain-boundary viscosities of iron-bearing and iron-free olivine. Overall, we consider that the newly observed mild dissipation peak is attributable to the micromechanical model of EAGBS. In support of this suggestion, the derived grain-boundary viscosity based on $\tau_P = \tau_e$ is broadly consistent with the other estimates of grain-boundary viscosity at high temperatures of 1200–1300 °C but diverges marked at lower temperatures because of the much higher activation energy.

4.5. *High activation energy in micro stress/strain testing*

The presence of high stress concentration at grain boundaries, caused by elastically accommodated grain boundary sliding, results in a spatial distribution of vacancy concentration. This leads to flux of vacancies/

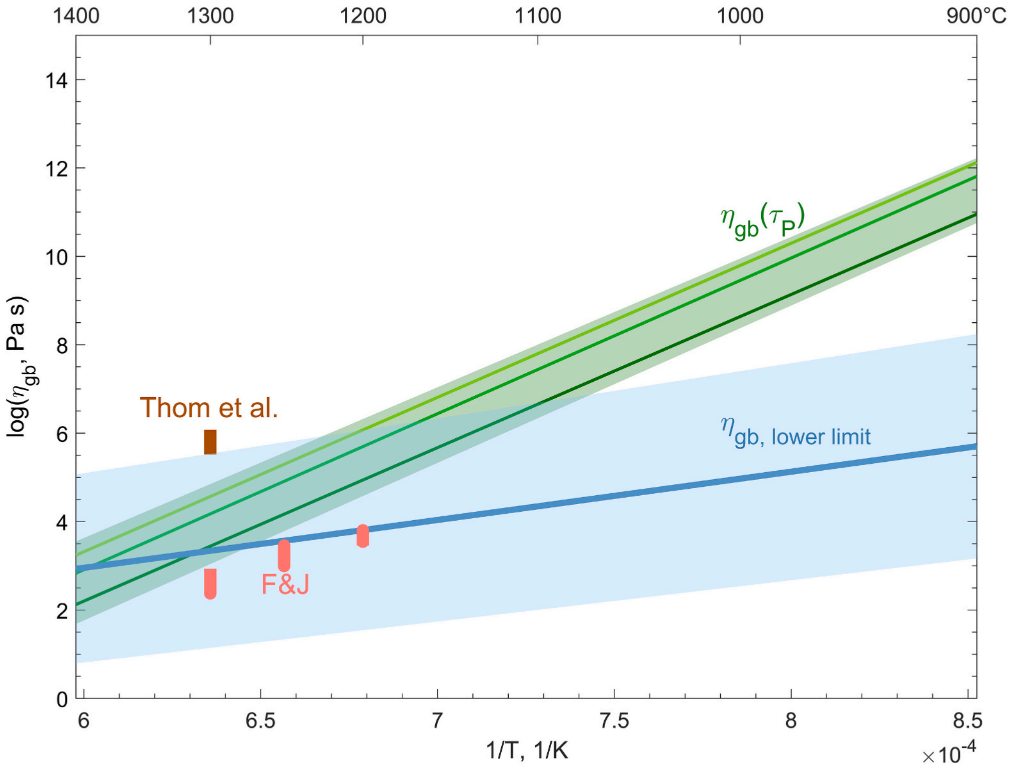

Fig. 9. Comparison among values of olivine grain-boundary viscosity η_{gb} calculated from τ_P in green, estimated from the Si boundary diffusivity in blue, derived from steady-state diffusional creep in red (Faul and Jackson, 2007), and experimentally measured in brown (Thom et al., 2020). From top to bottom, the three green lines were calculated based on the Burgers model parameters for run A1928 (d = 6.3 μm, log(τ_P, s) = 5.1 and E_P = 664 kJ/mol), A1906 (d = 6.5 μm, log(τ_P, s) = 4.8 and E_P = 671 kJ/mol), run A1802 (d = 3.7 μm, log(τ_P, s) = 3.7 and E_P = 660 kJ/mol) in Table 2. The upper and lower limits of $\eta_{gb}(\tau_P)$ confidence band were determined by the parameters and associated uncertainties for run A1928 and run A1802. The solid blue line for $\eta_{gb,\text{lower limit}}$ is calculated from Eqs. (4) and (5). The range of confidence band was determined by the uncertainties of exponential factor A_{gb} and activation energy E_{gb} from Fei et al. (2016). (For interpretation of the references to color in this figure legend, the reader is referred to the web version of this article.)

atoms through grains or along grain boundaries, which accommodates the strain incompatibility among grains. Such a process, known as or diffusionally assisted/accommodated grain-boundary sliding (DAGBS), involves two sequential steps: first, the creation of local gradient in vacancy concentration due to stress heterogeneity at crystal/grain interface requiring interfacial reaction, and second, the diffusive transport of the vacancies (Ashby, 1972). Typically, the disordered grain-boundary region is assumed to be a perfect sink/source for atoms and vacancies. Under these circumstances, the latter step of diffusive transport is rate controlling. If DAGBS is truly the dominant mechanism for high temperature background, activation energy *E* measured by large-strain diffusional creep testing should be consistent with the activation energy for viscoelastic relaxation occurring during forced-oscillation/creep testing at microstrain amplitude. Such broad consistency has previously been demonstrated in forced-oscillation studies in our laboratory (with the superseded experimental methodology) but the high activation energies of this study (consistently >600 kJ/ mol) require careful reconsideration.

Here we examine the possibility that the diffusion required for grain-boundary sliding under conditions of microstrain testing may be rate-limited by interfacial reaction involving a high activation energy. The assumption that the grain boundary is a perfect sink and source for vacancies during diffusional creep was relaxed by Ashby (1969), Greenwood (1970), Burton (1972) and Arzt et al. (1983) (reviewed by Karato, 2008, p.135) who suggested that at conditions of small stress and/or fine grain size, interfacial reaction can be rate-limiting. Interfacial-reaction-controlled creep has been frequently invoked to explain the discrepancy between the theory of diffusional creep and the results of creep testing on metals and ceramics (e.g. Gifkins, 1976; Cannon et al., 1980; Hsu et al., 1983; Sherby and Wadsworth, 1989; Cai et al., 1999; Nieh and Sherby, 2005, p.45).

A modest variation of activation energy with stress magnitude may also be found in the mechanical testing of organic rock analogue material (polycrystalline borneol) in the regime of diffusional creep. Microcreep testing with differential stress amplitude of 0.28 MPa reveals the value of activation energy as 101 kJ/mol (Takei et al., 2014). The Maxwell relaxation time obtained from such microcreep testing is used for normalization of dissipation and shear modulus data into master curves. However, the strain rates for diffusional creep testing on the same material with stress ranging from 0.3 to 1 MPa suggest an activation energy that is significantly lower at 70 kJ/mol (Fig. 7 from Sasaki et al., 2019).

The systematic exploration of creep testing on ultramafic geomaterials with low stress (< 10 MPa) has been limited thus far. Sundberg and Cooper (2008) found weakening of olivine-orthopyroxene mixture during creep with stress ~10 MPa at 1200 °C, which they attributed to interfacial-reaction-controlled creep facilitated by reaction at olivine-pyroxene phase boundaries. On the contrary, strengthening of forsterite-enstatite mixture and Fe-bearing olivine has been observed at similar high temperature with stress ≤10 MPa, demonstrating a convex shape of the $\log\dot{\varepsilon}$ vs $\log\sigma$ relation over a wide range of differential stresses from 4 to 144 MPa (Nakakoji et al., 2018; Yabe et al., 2020). Specimens of polycrystalline Fo_{90} olivine of ~1–4 μm grain size containing 0–30% En_{90} pyroxene were deformed by Yabe et al. (2020) at temperatures of 1150–1300 °C. For stresses <20–30 MPa, the strain rate became more stress- and temperature-sensitive. The optimal fit to the rheology within this low-stress regime was obtained with a higher value of the activation energy ~610 kJ/mol, cubic stress dependence and linear grain-size exponent. Further, they observe that with increasing stress, the activation energy, grain-size and stress dependence gradually approach the behavior commonly associated with diffusional creep.

Our torsional forced-oscillation tests involve a shear stress that increases with radial position within the specimen from zero on the torsional axis to a maximum value near ~0.5 MPa at its cylindrical surface - a range substantially lower than the stress identified by Yabe et al. (2020) for the transition between interfacial-reaction-controlled and diffusional creep. Accordingly, it seems reasonable to speculate that the influence of interfacial reaction on sources and sinks of vacancies might explain the high activation energy for grain-boundary diffusion indicated in the linear viscoelastic rheology observed in this study.

Similarly high activation energy (~700 kJ/mol) has been observed by in their forced-oscillation testing at ambient pressure of one polycrystalline olivine sample derived from natural precursor (Balsam Gap dunite from Jackson County, North Carolina)(Gribb and Cooper, 1998a). The high activation energy was tentatively attributed to segregation to grain boundaries of incompatible trace elements Ca or Al for diffusionally accommodated grain-boundary sliding, although, as noted in Section 4.4, the mechanical behavior may be influenced by the presence of a small melt fraction. Although the frame of their apparatus resides within the furnace, the apparatus response was apparently not independently calibrated by testing a reference sample at high temperature (Gribb and Cooper, 1998b), potentially complicating the measurement of activation energy. Despite the uncertainties sourced from their sample preparation and experimental methodology, much lower activation energy (~380 kJ/mol) for diffusional creep has been observed during creep testing of samples from the same origin prepared by similar approach, hence with almost the same chemical composition and fine grain sizes (Cooper and Kohlstedt, 1984). Other results from creep testing on samples from natural origin, therefore containing trace amount of chemical complexity, similarly also show relatively low activation energy in diffusional creep (e.g. Hirth and Kohlstedt, 1995; Karato et al., 1986). Trace element-free olivine deformed in diffusional creep prepared with the same sol-gel methods as used for this study yielded an activation energy of 485 kJ/mol (Faul and Jackson, 2007). Åheim dunite also revealed a contrast in activation energy from microstrain forced oscillation (~ 635–730 kJ/mol in Kampfmann and Berckhemer (1985)) and large-strain creep, although deformation occurred in the dislocation creep regime (~ 444 kJ/mol in Chopra and Paterson (1981)). Accordingly, these previously observed high activation energies from forced-oscillation testing on natural-precursor derived olivine cannot be solely explained by the chemical complexity within grain boundaries at temperature below 1300 °C.

Furthermore, for Ti-doped sol-gel-derived olivine polycrystals tested with our current forced-oscillation methodology under oxidizing/hydrous conditions within Pt liners, the activation energies (416–350 kJ/mol) are consistently lower than the activation energy (464 kJ/mol) for pure sol-gel olivine under the same conditions within Pt liners (Cline, 2018, PhD thesis). Within NiFe liner and hence under dry and more reducing conditions as in this study, the activation energy for Ti-doped olivine further increased to 504 kJ/mol, but still lower than the activation energy for undoped olivine (~ 660 kJ/mol) in this study. The systematic increment of activation energy associated with absence of Ti and dry/reducing conditions in these chemically well-controlled samples suggests that chemical complexity may actually lower the activation energy for viscoelastic relaxation in polycrystalline olivine.

Overall, these observations from forced-oscillation testing suggest that the activation energy can be highly sensitive to experimental methodology employed in sample preparation and mechanical testing. Therefore, although interfacial reaction during microstrain forced oscillation might potentially explain the observed contrast in activation energies of this study and of diffusional creep, we need additional forced-oscillation and microcreep tests on both pure and chemically more complex dunite samples for a definitive interpretation.

4.6. Geophysical implications

The updated experimental results described here confirm that dry, melt-free and fine-grained dunite begins to deviate from purely elastic behavior at about 900 °C at the experimental frequency range. The analysis of anelastic relaxation in the tested samples has demonstrated that Δ_p, the relaxation strength associated with elastically accommodated grain-boundary sliding (EAGBS), now better constrained at a value of 0.02 ± 0.01 (Table 2), is substantially less than that (0.06) of Jackson and Faul (2010). Accordingly, the modulus deficit is only ~2% accompanied by a subtle perturbation to the period-dependence of dissipation at $\log Q^{-1} \sim -2$. This reduced relaxation strength for EAGBS is important for the interpretation of seismological models of the oceanic lithosphere-asthenosphere boundary (LAB).

Karato (2012) suggested that the relaxation time τ_P associated with EAGBS might vary strongly with water content. Under these circumstances, it was suggested that τ_P might exceed seismic periods within the relatively dry lithosphere resulting in conditions unrelaxed with respect to EAGBS. Contrasting relaxed conditions, with τ_P less than seismic periods, might prevail within the hydrous asthenosphere. With sufficient (water-independent) relaxation strength for elastically accommodated grain-boundary sliding, a sharp decrease in shear wave velocity (by 5–10% within 10–15 km) at the depth of 60–70 km within the oceanic upper mantle, has thus been attributed to water-mediated elastically accommodated grain-boundary sliding (Karato, 2012). However, with the lower relaxation strength for EAGBS determined in this study, the transition invoked by Karato (2012) from dry, unrelaxed conditions within the lithosphere to hydrous, relaxed conditions in the asthenosphere cannot explain the seismically observed large velocity reduction associated with the LAB.

Direct experimental studies of the influence of water on low-strain viscoelastic relaxation in fine-grained peridotite have yielded conflicting results as follows. Aizawa et al. (2008) reported the results of low-strain ($<10^{-5}$) torsional forced-oscillation tests on specimens of Anita Bay dunite mylonite, either pre-fired or subject to in situ dehydration of a hydrous fluid phase within a sealed Pt capsule. Substantially enhanced dissipation and modulus dispersion were observed in the specimen subjected to in situ dehydration that yielded ~2 vol% of an aqueous fluid phase. However, the interpretation of the data from samples cored from as received rocks is complicated by the presence of melt (Aizawa et al., Fig. 7; in excess of 5% locally), substantial heterogeneity of phase distributions (pyroxenite to dunite) and grain size. (~ 50 μm ground mass and > mm size porphyroclasts). Subsequent experiments in our laboratory on synthetic Ti-doped Fo_{90} and Fo_{100} polycrystals, and reconstituted San Carlos Fo_{90} olivine, tested within mild-steel jackets variously lined with Pt, Ni, or $Ni_{70}Fe_{30}$ foil were reported by Cline et al. (2018). Alternative use of the $Ni_{70}Fe_{30}$ and Pt liners provided access to contrasting reducing/dry, and oxidizing/hydrous conditions, respectively. Intermediate redox conditions were provided by the use of Ni foil. The dissipation and dispersion were similarly markedly enhanced, relative to those obtained under reducing/dry conditions, for all iron-bearing specimens tested under the oxidizing and hydrous conditions, irrespective of the concentration of the dominant $\{Ti^{\bullet\bullet}_{Mg}(2H)''_{Si}\}^{\times}$ defect. The Ti-doped Fo_{100} specimen, containing substantial concentrations of both $\{Ti^{\bullet\bullet}_{Mg}(2H)''_{Si}\}^{\times}$ and $(4H)^{\times}_{Si}$ defects and tested under oxidizing/hydrous conditions, showed no such enhancement of the viscoelastic relaxation. Accordingly, it was concluded that the enhanced relaxation in the Fe-bearing specimens is attributable to the difference in oxygen fugacity rather than the presence of water.

An alternative view of the role of water comes from recent axial stress-oscillation experiments conducted at 3 GPa confining pressure within solid-medium high-pressure apparatus (Liu et al., 2023). Fine-grained Fo_{100} polycrystals were tested during cooling from 1100 to

950 °C at much higher strain amplitudes $\sim 10^{-3}$ than those of the ANU laboratory but surprisingly still apparently within the linear regime. The specimens contained 9 to 143 wt ppm H_2O, accommodated mainly in the $(4H)^{\times}_{Si}$ defect - as expected in the absence of Ti and at the relatively high pressure of this study (Muir et al., 2022). Liu et al. (2023) reported the presence of a short-period (1–10 s) dissipation peak superimposed upon the dissipation background, along with related modulus dispersion. The relaxation strength Δ_P associated with the dissipation peak was found to increase systematically and almost linearly with the concentration of water, but its centre period τ_P was insensitive to the variation of grain size, leading the authors to conclude that the peak cannot be associated with grain-boundary sliding. That τ_P is also insensitive to water concentration is inconsistent with the suggestion by Karato (2012). More puzzling is the insensitivity of the peak period to temperature which seems to exclude any possibility of a thermally activated relaxation process. The presence of a water-related dissipation peak in this study appears to directly contradict the observation by Cline et al. (2018) of no significant enhancement of viscoelastic relaxation in Fo_{100}:Ti tested under oxidizing/hydrous conditions involving the presence of both $\{Ti^{\bullet\bullet}_{Mg}(2H)''_{Si}\}^{\times}$ and $(4H)^{\times}_{Si}$ defects. Further experimental work on the influence of water, well beyond the scope of the present study, will be required to resolve this discrepancy.

Further quantitative analysis of the implications of the mild dissipation peak superimposed on the background for the interpretation of upper-mantle seismological models requires a well-constrained grain-size sensitivity of viscoelastic relaxation of dunite, currently being measured with the modern experimental methodology.

5. Conclusion

The experimental methodology employed in microstrain forced-oscillation testing in our laboratory has been upgraded progressively over the past decade by removal of interfacial NiFe foils within the specimen assembly and replacement of a polycrystalline alumina control specimen by single-crystal sapphire (Jackson et al., 2014; Cline et al., 2018). With this improved experimental methodology, we have conducted forced-oscillation testing on a suite of dry and melt-free fine-grained synthetic dunite samples within mild-steel, and alternative copper and stainless-steel jacket materials. The improvement in experimental methodology leads to improvement of the quality of the data and changed fit parameters, and the data newly obtained for stainless-steel-jacketed olivine reveal negligible strain-energy dissipation and modulus dispersion below 900 °C. The contrasting significant levels of dissipation and modulus relaxation at 850–750 °C obtained in this and previous studies employing mild-steel jackets are therefore most likely an artifact associated with the austenite-ferrite phase transition in the mild-steel jackets.

Regardless of the difference in annealing temperature and jacket material, a mild dissipation peak in melt-free, dry and fine-grained dunite was newly and consistently observed at higher temperatures (~950–1050 °C) within the observational window, attributable to elastically accommodated grain-boundary sliding during the onset of anelastic relaxation. The relaxation strength associated with the newly observed dissipation peak is experimentally observed to be only a few percent of the relaxation strength of dissipation background. The seismological impact of elastically accommodated grain-boundary sliding will therefore be confined to minor (~2%) relaxation of the shear modulus and an associated modest perturbation to the frequency dependence of seismic wave attenuation. Accordingly, elastically accommodated grain-boundary sliding and its sensitivity to the concentration of water may have insufficient leverage on wave speeds and attenuation to account for seismological observations of the lithosphere-asthenosphere boundary in the Earth's upper mantle.

CRediT authorship contribution statement

Tongzhang Qu: Conceptualization, Data curation, Formal analysis, Investigation, Methodology, Validation, Visualization, Writing – original draft. **Ian Jackson:** Conceptualization, Data curation, Formal analysis, Funding acquisition, Investigation, Methodology, Project administration, Resources, Supervision, Validation, Visualization, Writing – review & editing. **Ulrich H. Faul:** Conceptualization, Data curation, Formal analysis, Funding acquisition, Investigation, Methodology, Supervision, Writing – review & editing. **Emmanuel C. David:** Data curation, Investigation, Methodology.

Declaration of competing interest

The authors declare that they have no known competing financial interests or personal relationships that could have appeared to influence the work reported in this paper.

Data availability

The forced-oscillation data have been uploaded in supplementary data in Appendix C.

Acknowledgement

We are grateful for technical assistance from Hayden Miller of the Research School of Earth Sciences and Dr. Frank Brink of the NCRIS-supported Centre for Advanced Microscopy at the Australian National University. We acknowledge financial support from the Australian Research Council grant DP200100824. This paper was substantially improved in response to constructive criticism by Professor Shun-ichiro Karato and an anonymous reviewer.

Appendix A. Results for copper-jacketed olivine

The use in forced-oscillation studies of copper as an alternative to the routinely used mild-steel jacket material was first reported by Jackson et al. (2014). In that study, a synthetic Fo_{90} polycrystal (H6585), first tested within an $Ni_{70}Fe_{30}$-lined mild-steel jacket in run A1127, was reground, refired and tested, with a mean grain size of 10.7 μm, within a bare Cu jacket in run A1382. Tentative evidence was presented of a dissipation peak with relaxation strength ~0.02 located near 10 s period at the maximum temperature of 900 °C (Jackson et al., 2014). Subsequently, a more comprehensive study of copper-jacketed olivine has been undertaken with a newly hot-pressed specimen H6788 tested to a maximum temperature of 1050 °C (run A1464), closely approaching the 1084 °C melting point of copper. Complementary studies of polycrystalline copper and of copper-jacketed sapphire have also been conducted (David and Jackson, 2018). Microstructural information for the specimen of run A1464 is presented in. Fig. A1 showing the coarse-grained copper jacket enclosing a fine-grained olivine polycrystal of mean grain size 4.6 μm.

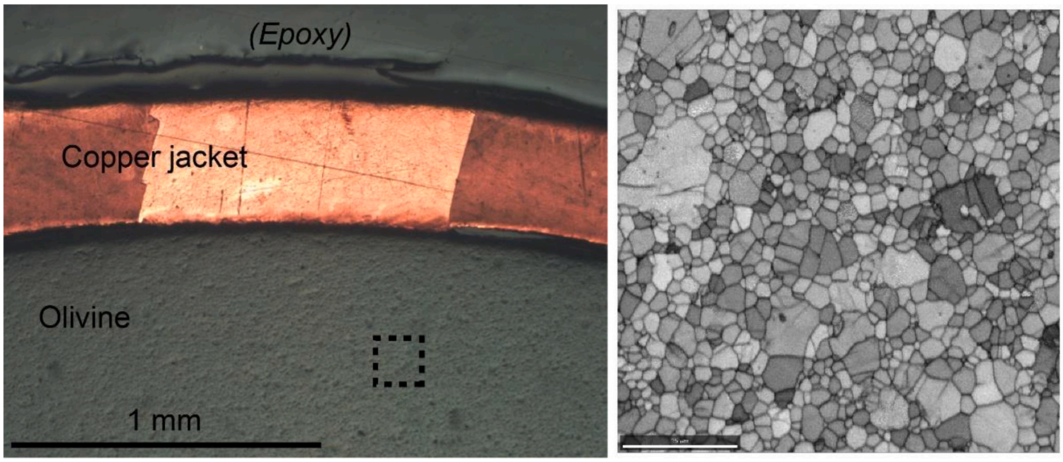

Fig. A1. (a) Reflected light micrograph of the Cu-jacketted Fo_{90} olivine specimen recovered from run 1464. (b) Band-contrast map from electron backscattered diffraction imaging of the olivine microstructure (scale bar: 25 μm, mean grain size: 4.6 μm).

The shear modulus and associated strain-energy dissipation measured at the highest temperatures (1050–900 °C) of run A1464 and those at the highest temperature (900 °C) of the run A1382 (Jackson et al., 2014) are compared in Fig. A2 with the optimal Burgers model (Table 2) for the SS-jacketed olivine of run 1802.

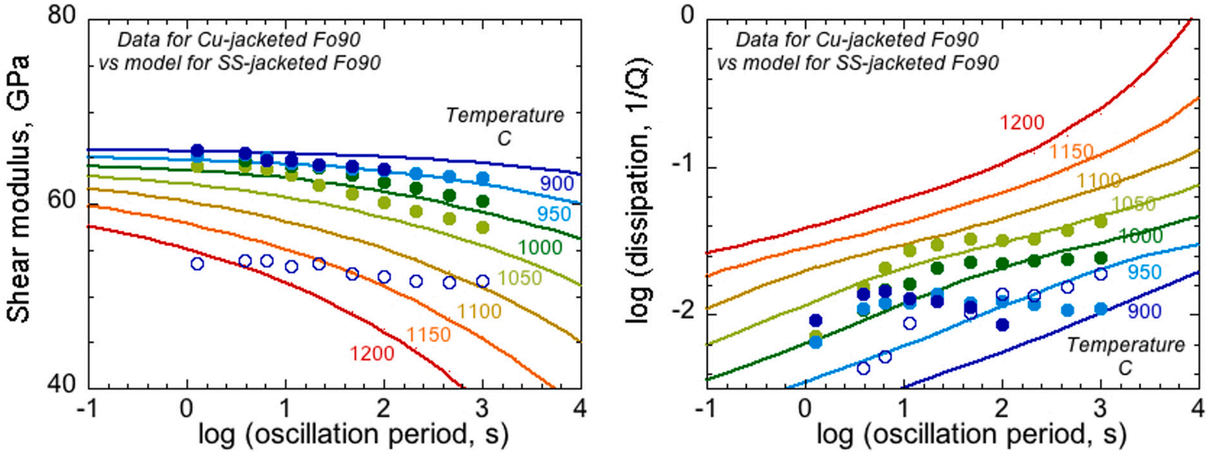

Fig. A2. Comparison of data for Cu-jacketted fine-grained olivine specimens at the highest temperatures (1050–900 °C) of run A1464 (solid symbols) and run A1382 (open symbols, Jackson et al., 2014, reprocessed) with the optimal Burgers 'background + peak' model for SS-jacketted olivine from run A1802 of the present study.

It proved impossible to achieve a completely satisfactory fit of a Burgers 'background + peak' model to the full dataset for run A1464 spanning the temperature range 1050–550 °C. Accordingly, we here restrict our attention to the (G, Q^{-1}) data obtained at the highest temperatures (1050 °C $\geq T \geq$ 900 °C). The systematic reduction in background dissipation on staged cooling from 1050 °C to 950 °C, associated with a high activation energy of ~670 kJ/ mol comparable with those of Table 2, reveals progressively more clearly a pronounced dissipation peak located near 10 s period across this temperature interval. At 900 °C, the dissipation is dominated by the peak of amplitude $\log Q^{-1} \sim -1.9$, broadly consistent with the results of the earlier exploratory study of the somewhat more coarse-grained (10.7 μm) specimen to a maximum temperature of 900 °C (Jackson et al., 2014). On cooling below 900 °C in run A1464 (not plotted in Fig. A2), the dissipation peak increases somewhat in amplitude from $\log Q^{-1} \sim -1.9$ to $\log Q^{-1} \sim -1.6$, and begins to move steadily towards longer periods, as expected for a thermally activated process.

Close comparison of the data newly obtained for olivine jacketed within mild steel and stainless steel with that for Cu-jacketed olivine is thus complicated by some uncertainties in the 'Cu' dataset, mainly attributed to the fact that it was limited to temperatures ≤1050 °C approaching the melting point of copper. This limitation meant that the usual procedure of annealing the assembly at the highest temperature prior to data acquisition may have been less satisfactory for minimizing any interfacial compliance. Moreover, the close approach to the melting point involved very intense viscoelastic relaxation resulting in very strong, and strongly temperature-dependent, modulus dispersion and dissipation in the Cu jacket, with values of G and $\log Q^{-1}$ reaching 4 GPa and 0.1, respectively, at 1000 s period and 1050 °C. Nevertheless, the peak in olivine dissipation measured at the highest temperatures (1050 and 1000 °C) of run A1464 is broadly consistent with that in the Burgers model for run A1802 on SS-jacketed Fo_{90} of similar grain size.

Appendix B. Improved experimental methodology

The torsional oscillation techniques of our laboratory, like forced–oscillation techniques more generally, require coupling between the specimen and the loading system. In our high-pressure apparatus, the interface between the lapped surface of the alumina torsion rod and the adjacent specimen is subject to a normal stress equal to the confining pressure (200 MPa) that provides for frictional coupling. It is important to document and minimize any contribution to the torsional compliance of the assembly associated with such coupling.

Experimental procedures employed in our laboratory have evolved over many years and have recently been further refined. $Ni_{70}Fe_{30}$ ('NiFe') foils of 70 μm thickness have traditionally been used at each end of the specimen in order to provide chemical isolation between specimen and high-grade Lucalox™ alumina torsion rods, minimize interfacial stresses arising from the mismatch in thermal expansion between specimen and torsion rods, and help maintain appropriate redox conditions for Fo_{90} olivine (e.g., Jackson et al., 2002). The contribution of such foils to the torsional compliance of the assembly was assumed to be negligible until the torsional compliances of alternative foil-free and foil-bearing reference assemblies were compared (Jackson et al., 2009). Reference assemblies containing a Lucalox™ alumina control specimen and two foils – either one at each end of the control specimen ('2f') or paired at one end (double-foil: 'df') – were found to be significantly more compliant in torsion than the corresponding foil-free ('ff') reference assembly. Moreover, the phase lag of the torsional distortion of the reference assembly, relative to that for the elastic element, was shown to be proportional to the number of foil-alumina interfaces. It therefore became our standard practice to compare the compliance for a specimen assembly containing two foil-alumina interfaces with that for the double-foil reference assembly, similarly containing two foil-alumina interfaces. We also implemented a model for the viscoelastic behavior of the alumina control specimen involving extrapolation of published data for more fine-grained polycrystalline alumina. However, this improved procedure was not without residual difficulties. Data for relatively coarse-grained and therefore not very dissipative specimens, tested at temperatures of 1200–1300 °C and oscillation periods >10–30 s, showed an unphysical negative dependence of Q^{-1} upon period (Jackson et al., 2009).

Accordingly, we have recently made further changes. The polycrystalline alumina control specimen has been replaced by a sapphire single-crystal control specimen oriented with [0001] parallel with the torsional axis (Jackson et al., 2014), that is reasonably modeled as elastic at temperatures as high as 1300 °C. The other significant refinement of our experimental procedure is to abandon the longstanding use of an NiFe foil at each end of the specimen and a double-foil at one end of the control specimen (Jackson et al., 2009), in favor of their direct contact with the torsion rods of Lucalox™ alumina (Jackson et al., 2014). It has been demonstrated that appropriate redox conditions are adequately maintained by foil wrapping of the cylindrical surface of the specimen (Cline et al., 2018). Localized chemical reaction occurring at the direct contact thus established between the alumina torsion rods and synthetic dunite specimens, and its likely impact upon the torsional compliance are described below.

B.1. Impact of the improved experimental methodology: minimizing the interfacial compliance

The effect of the most recent changes in experimental methodology is illustrated in Fig. B1 by comparing the key steps in data processing between the now superseded and current methodologies. In order to eliminate the contribution from the torsion rods common to the compliances of the specimen and reference assemblies, we routinely subtract from the complex torsional compliance S_{spc} of the specimen assembly that (S_{ref}) of the chosen reference assembly. All such compliances are made dimensionless by division by the known compliance of the hollow-steel elastic element maintained at room temperature and exposed to the same torque. The result $S_{rel} = S_{spc} - S_{ref}$, with adjustment to S_{cor} for any minor geometric differences between the specimen and reference assemblies, is the difference in normalized compliance between the jacketted specimen and the jacketted control specimen. Accordingly, S_{cor} is then added to S_{jc}, the calculated compliance for the jacketted control specimen, to obtain $S_{jr} = S_{jc} + S_{cor}$, the compliance of the jacketed specimen. Finally, the torsional stiffness S_j^{-1} of the jacket (inclusive of any metal liner) is subtracted from the dimensional stiffness S_{jr}^{-1} of the jacketed specimen to obtain the torsional stiffness S_r^{-1} of the specimen itself from which the shear modulus G and dissipation Q^{-1} are calculated.

The role of the metal foils within the superseded methodology is highlighted by focusing attention on the triangles representing the vector subtraction $S_{rel} = S_{spc} - S_{ref}$ at the longest oscillation period (1000 s) and the highest routinely accessed temperature of 1200 °C (Fig. B1). The vector S_{ref} in Fig. B1(a) for the *df* foil-bearing reference assembly of the superseded methodology is inclined at a large angle below the real axis. This results not from the viscoelasticity of the foil material, but from the two alumina-foil interfaces within the assembly (Jackson et al., 2009). In marked contrast, the absence of foils from the reference assembly in the current methodology (Fig. B1b) results in close alignment of the S_{ref} vector with the real axis.

Thus, even at the longest oscillation period of 1000 s, and the highest routinely accessed temperature of 1200 °C, the measured compliance of the stainless steel-jacketted sapphire reference assembly remains almost real (i.e. elastic), clearly demonstrating the absence of a substantial interfacial contribution to the compliance. Further analysis of the performance of the stainless steel-jacketed sapphire reference assembly has involved calculation of its torsional compliance from the known geometry and material properties of its sapphire, Lucalox alumina, stainless-steel, and EN25 steel components. Comparison of this model compliance with that measured in run A1789 reveals a small difference, displayed on a greatly expanded scale in Fig. B1c, that is attributed either to the bare interface between alumina and sapphire, or to underestimation of the extent of viscoelastic relaxation in the alumna torsion rods.

For the specimen assembly employed in the current methodology, the chemical reaction described below across the direct contact between olivine specimen and alumina torsion rods results in the formation of a refractory crystalline assemblage, amounting to a reaction bond, expected to be similarly of low compliance. Thus, uncertainties associated with interfacial compliance involving the NiFe foils and with the viscoelastic behavior of the polycrystalline alumina control specimen have now been effectively eliminated. This represents a marked improvement over the previous methodology where it was necessary to assume that the relatively large compliance associated with alumina-foil interfaces was reproducible between assemblies.

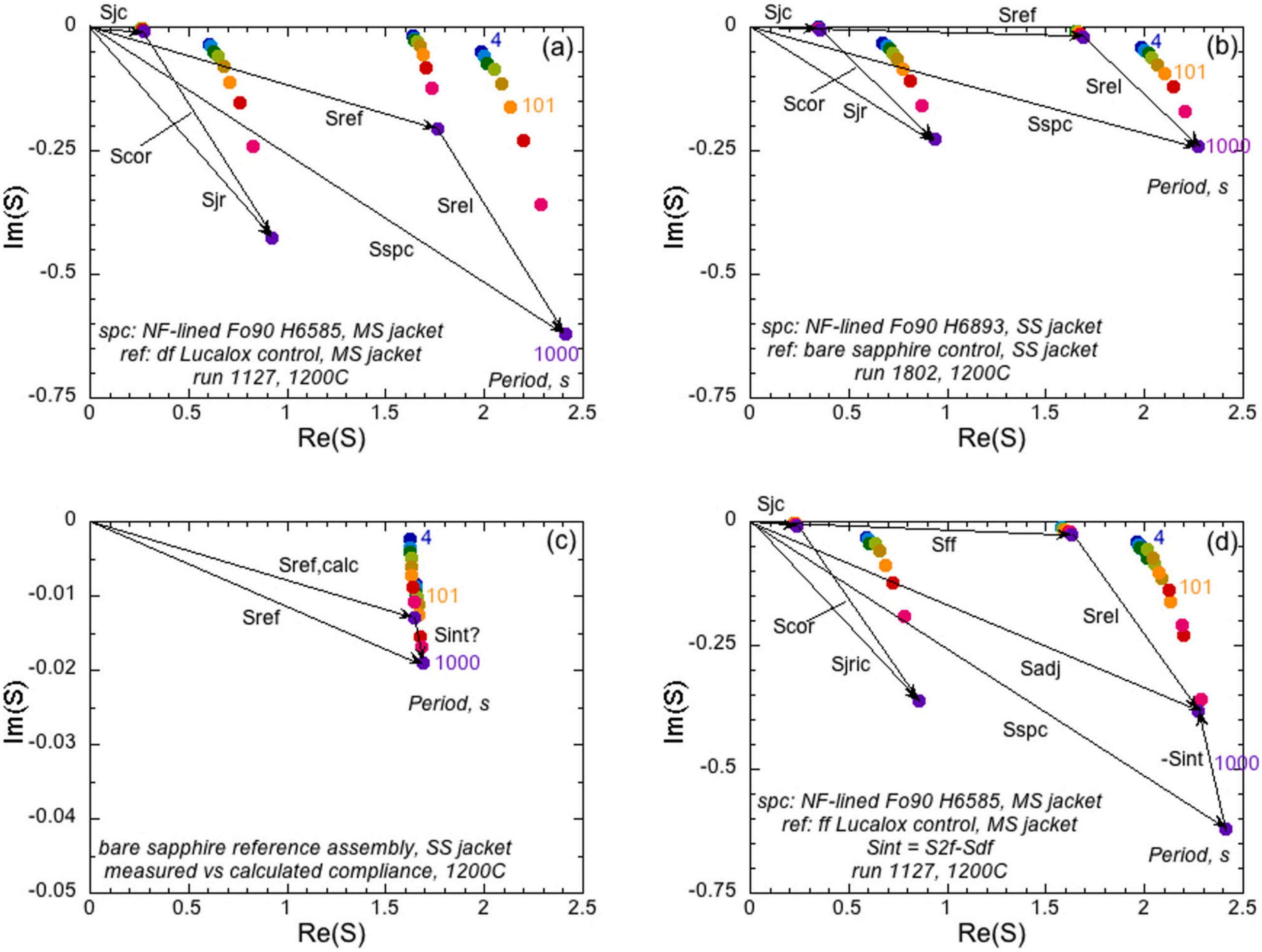

Fig. B1. The impact of the recent refinement of experimental methodology upon data processing to obtain the torsional compliance S_{jr} of the jacketted synthetic rock specimen, as explained in the text. (a) Data obtained at 1200 °C and oscillation periods of 4–1000 s in run A1127 with the superseded methodology involving use of an NiFe foil at each end of the synthetic dunite specimen H6585 of 3.6 μm average grain size (H refers to the precursor hotpressed specimen, A to the tested specimen. The grain size is that after testing.). These data are compared with those for a double-foil reference assembly with a Lucalox alumina control specimen. (b) Data obtained under the same conditions in run A1802 with the recently refined methodology. A specimen assembly containing a synthetic dunite specimen H6893 of 3.7 μm grain size within an NiFe-lined stainless-steel jacket is compared with a reference assembly involving a stainless steel-jacketted sapphire control specimen in direct contact with alumina torsion rods. (c) A comparison at 1200 °C of the compliance calciulated for the sapphire reference assembly with that actually measured in run A1789. Note that the scale for the y-axis has been expanded 15-fold relative to that of panel (b). (d) The data of run 1127 (Fig. B1a), corrected for interfacial compliance with $S_{int} = S_{2f} - S_{df}$, and then compared with the compliance of the foil-free (ff) reference assembly.

Comparison between Fig. B1(a) and (b) suggests an alternative approach to the processing of data for foil-bearing specimen assemblies as follows. The compliance differential $S_{int} = S_{2f} - S_{df}$ between the *2f* and *df* reference assemblies, interpreted as the compliance of a pair of alumina-foil interfaces, can be used to adjust the compliance of the foil-bearing specimen assembly for the influence of its two alumina-foil interfaces. The compliance $S_{adj} = S_{spc} - S_{int}$ of the specimen assembly adjusted in this way, can then be compared with that (S_{ff}) of the foil-free reference assembly, as shown in Fig. B1(d). The value of S_{jric} thus corrected for foil-related interfacial compliance is accordingly

$$S_{jric} = S_{jcff} + S_{rel} = S_{jcff} + S_{adj} - S_{ff} = S_{jcff} + S_{spc} - S_{int} - S_{ff} = S_{spc} + S_{jcff} - S_{2f} + S_{df} - S_{ff}$$

to be compared with that of the superseded approach (Fig. B1a) given by

$$S_{jr} = S_{jcdf} + S_{rel} = S_{jcdf} + S_{spc} - S_{df}.$$

The difference between these two quantities can be written as

$$S_{jric} - S_{jr} = \left(S_{df} - S_{ff}\right) - \left(S_{jcdf} - S_{jcff}\right) - \left(S_{2f} - S_{df}\right).$$

The final term in parentheses on the right provides an estimate of the compliance of a pair of alumina-foil interfaces. The compliance differential between the jacketed foil wrapped *df* control specimen of 11.50 mm diameter and the jacketted bare *ff* control specimen of 12.00 mm diameter should contribute equally to each of the first two terms. Accordingly, the difference between the first two terms provides a second estimate of the compliance of a pair of alumina-foil interfaces. Thus, if the compliances of all alumina-foil interfaces were identical, the difference S_{jric} - S_{jr} would be zero. The values of the interface-corrected compliance S_{jric} (Fig. B1d) have been compared with those of S_{jr} (Fig. B1a) resulting from the usual direct comparison with the *df* reference assembly. Although broadly similar, the values of S_{jric} are significantly more scattered than those of S_{jr}, presumably reflecting the propagation of errors associated with the data for the additional *ff* and *2f* reference assemblies.

B.2. Chemical reaction at the interface between dunite specimen and alumina torsion rod

After cooling from high temperature following the conduct of forced-oscillation testing, the alumina pistons have been observed to be firmly bonded to the synthetic dunite specimens. A section across such a bond was cut parallel to the axis of cylindrical sample from the assembly recovered after cooling from 1300 °C in run A1928, and polished as explained in Section 2.3. The backscattered electron image (Fig. B2a) shows three distinct grayscale regions, separated by boundaries oriented parallel with the interface. The EDS analysis of the left-most layer in Fig. B1b shows ∼70% Al_2O_3 with some MgO and FeO and no SiO_2. This is consistent with a spinel composition. The central region is enriched with SiO_2 (52%) 33% MgO, 8% Al_2O_3 and 6% FeO, consistent with a pyroxene composition. To the right is the unmodified Fo_{90} composition as expected. The layers of ∼10 μm width of spinel composition on the piston side of the interface, and of pyroxene composition on the olivine side, are inferred to result from the chemical reaction:

$$\text{alumina} + \text{olivine} = \text{pyroxene} + \text{spinel}$$

The mechanical influence of this thin, and refractory, reaction zone between alumina and olivine is expected to be negligible. The absence of any discontinuous decrease in shear modulus during staged cooling to 400 °C under 200 MPa pressure suggests that the cracking evident in Fig. B2a must have occurred during subsequent cooling and/or decompression.

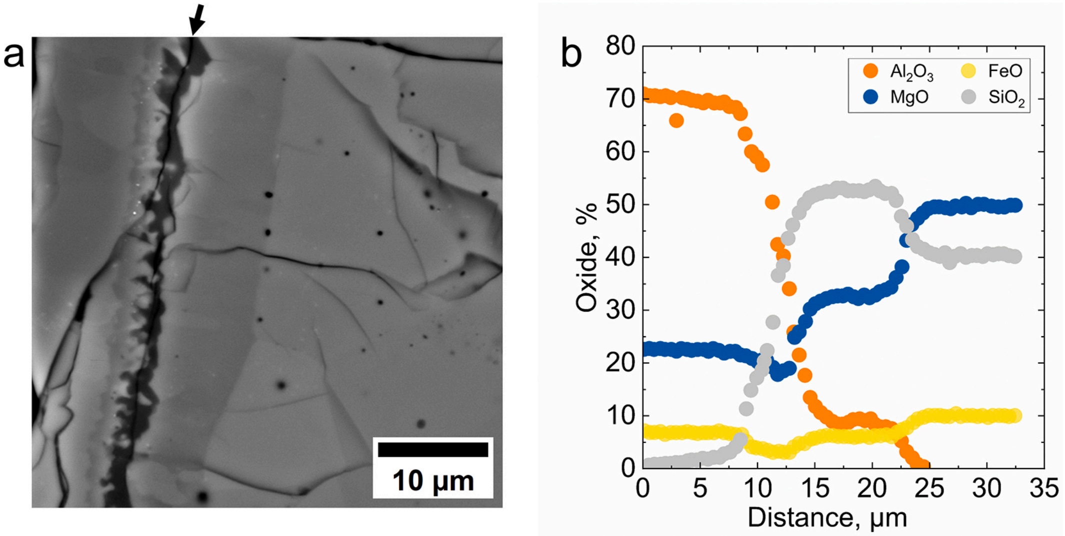

Fig. B2. (a) Backscattered electron image of the interface (indicated by the arrow) between the dunite specimen on the right and the Lucalox™ alumina alumina piston to the left. (b) Compositional profile across the specimen-piston interface.

Appendix C. Supplementary data

Supplementary data to this article can be found online at https://doi.org/10.1016/j.pepi.2024.107160.

References

Aizawa, Y., Barnhoorn, A., Faul, U.H., Fitz Gerald, J.D., Jackson, I., Kovács, I., 2008. Seismic properties of Anita Bay dunite: an exploratory study of the influence of water. J. Petrol. 49 (4), 841–855. https://doi.org/10.1093/petrology/egn007.

Alcock, C.B., Zador, S., 1967. Thermodynamic study of the manganese/ manganous-oxide system by the use of solid oxide electrolytes. Electrochim. Acta 12 (6), 673–677. https://doi.org/10.1016/0013-4686(67)85035-7.

Anderson, D.L., Given, J.W., 1982. Absorption band Q model for the Earth. J. Geophys. Res. Solid Earth 87 (1), 3893–3904.

Arzt, E., Ashby, M.F., Verrall, R.A., 1983. Interface controlled diffusional creep. Acta Metall. 31 (12), 1977–1989. https://doi.org/10.1016/0001-6160(83)90015-9.

Ashby, M.F., 1969. Boundary defects and the mechanism of particle movement through crystals. Scr. Metall. 3 (11), 843–848. https://doi.org/10.1016/0036-9748(69)90192-6.

Ashby, M.F., 1972. Boundary defects, and atomistic aspects of boundary sliding and diffusional creep. Surf. Sci. 31, 498–542. https://doi.org/10.1016/0039-6028(72)90273-7.

Barnhoorn, A., Jackson, I., Fitz Gerald, J.D., Kishimoto, A., Itatani, K., 2016. Grain size-sensitive viscoelastic relaxation and seismic properties of polycrystalline MgO. J. Geophys. Res. Solid Earth 121 (7), 4955–4976. https://doi.org/10.1002/2016JB013126.

Burton, B., 1972. Interface reaction controlled diffusional creep: a consideration of grain boundary dislocation climb sources. Mater. Sci. Eng. 10 (C), 9–14. https://doi.org/10.1016/0025-5416(72)90060-2.

Cai, B., Kong, Q.P., Lu, L., Lu, K., 1999. Interface controlled diffusional creep of nanocrystalline pure copper. Scr. Mater. 41 (7), 755–759. https://doi.org/10.1016/S1359-6462(99)00213-4.

Cannon, R.M., Rhodes, W.H., Heuer, A.H., 1980. Plastic deformation of fine-grained alumina (Al2O3): I, interface-controlled diffusional creep. J. Am. Ceram. Soc. 63 (1–2), 46–53. https://doi.org/10.1111/j.1151-2916.1980.tb10648.x.

Cantwell, P.R., Tang, M., Dillon, S.J., Luo, J., Rohrer, G.S., Harmer, M.P., 2014. Grain boundary complexions. Acta Mater. 62, 1–48. https://doi.org/10.1016/j.actamat.2013.07.037.

Chopra, P.N., Paterson, M.S., 1981. The experimental deformation of dunite. Tectonophysics 78 (1–4), 453–473. https://doi.org/10.1016/0040-1951(81)90024-X.

Cline, C.J.I., 2018. Viscoelastic Relaxation in Olivine: An Experimental Study of Alternative Mechanisms.

Cline, C.J., Jackson, I., 2016. Relaxation of the bulk modulus in partially molten dunite? Geophys. Res. Lett. 43 (22), 11,644–11,651. https://doi.org/10.1002/2016GL071004.

Cline, C.J., Faul, U.H., David, E.C., Berry, A.J., Jackson, I., 2018. Redox-influenced seismic properties of uppermantle olivine. Nature 555 (7696), 355–358. https://doi.org/10.1038/nature25764.

Cooper, Reid F., 2002. Seismic wave attenuation: energy dissipation in viscoelastic crystalline solids. Rev. Mineral. Geochem. 51 (January 2002) https://doi.org/10.2138/gsrmg.51.1.253.

Cooper, R.F., Kohlstedt, D.L., 1984. Solution-precipitation enhanced diffusional creep of partially molten olivine-basalt aggregates during hot-pressing. Tectonophysics 107 (3–4), 207–233. https://doi.org/10.1016/0040-1951(84)90252-X.

Cordier, P., Demouchy, S., Beausir, B., Taupin, V., Barou, F., Fressengeas, C., 2014. Disclinations provide the missing mechanism for deforming olivine-rich rocks in the mantle. Nature 507 (7490), 51–56. https://doi.org/10.1038/nature13043.

Dalton, C.A., Faul, U.H., 2010. The oceanic and cratonic upper mantle: clues from joint interpretation of global velocity and attenuation models. Lithos 120 (1–2), 160–172. https://doi.org/10.1016/j.lithos.2010.08.020.

David, E.C., Jackson, I., 2018. High-temperature internal friction and dynamic moduli in copper. Mater. Sci. Eng. A 730 (October 2017), 425–437. https://doi.org/10.1016/j.msea.2018.05.093.

Drury, M.R., Fitz Gerald, J.D., 1996. Grain boundary melt films in an experimentally deformed olivine-orthopyroxene rock: implications for melt distribution in upper mantle rocks. Geophys. Res. Lett. 23 (7), 701–704. https://doi.org/10.1029/96GL00702.

Farla, R.J., Jackson, I., Gerald, J.D.F., Faul, U.H., Zimmerman, M.E., 2012. Dislocation damping and anisotropic seismic wave attenuation in Earth’s upper mantle. Science 336 (April), 332–335.

Faul, U.H., Fitz Gerald, J.D., 1999. Grain misorientations in partially molten olivine aggregates: an electron backscatter diffraction study. Phys. Chem. Miner. 26 (3), 187–197. https://doi.org/10.1007/s002690050176.

Faul, U.H., Jackson, I., 2007. Diffusion creep of dry, melt-free olivine. J. Geophys. Res. Solid Earth 112 (4), 1–14. https://doi.org/10.1029/2006JB004586.

Faul, U.H., Fitz Gerald, J.D., Jackson, I., 2004. Shear wave attenuation and dispersion in melt-bearing olivine polycrystals: 2. Microstructural interpretation and seismological implications. J. Geophys. Res. Solid Earth 109 (B6). https://doi.org/10.1029/2003JB002407.

Faul, U.H., Cline, C.J., Berry, A., Jackson, I., Garapić, G., 2018. Constraints on oxygen fugacity within metal capsules. Phys. Chem. Miner. 45 (6), 497–509. https://doi.org/10.1007/s00269-017-0937-7.

Fei, H., Koizumi, S., Sakamoto, N., Hashiguchi, M., Yurimoto, H., Marquardt, K., et al., 2016. New constraints on upper mantle creep mechanism inferred from silicon grain-boundary diffusion rates. Earth Planet. Sci. Lett. 433, 350–359. https://doi.org/10.1016/j.epsl.2015.11.014.

Frost, H.J., Ashby, M.F., 1982. Deformation-Mechanism Maps: The Plasticity and Creep of Metals and Ceramics. Pergamon Press.

Fujino, K., Sasaki, S., Takéuchi, Y., Sadanaga, R., 1981. X-ray determination of electron distributions in forsterite, fayalite and tephroite. Acta Crystallogr. B Struct. Crystallogr. Cryst. Chem. 37 (3), 513–518. https://doi.org/10.1107/S0567740881003506.

Gifkins, R.C., 1976. Grain-boundary sliding and its accommodation during creep and superplasticity. Metall. Trans. A. 7 (8), 1225–1232. https://doi.org/10.1007/BF02656607.

Greenwood, G.W., 1970. The possible effects on diffusion creep of some limitation of grain boundaries as vacancy sources or sinks. Scr. Metall. 4 (3), 171–173. https://doi.org/10.1016/0036-9748(70)90187-0.

Gribb, T.T., Cooper, R.F., 1998a. A high-temperature torsion apparatus for the high-resolution characterization of internal friction and creep in refractory metals and ceramics: application to the seismic-frequency, dynamic response of Earth’s upper mantle. Rev. Sci. Instrum. 69 (2), 559–564. https://doi.org/10.1063/1.1148694.

Gribb, T.T., Cooper, R.F., 1998b. Low-frequency shear attenuation in polycrystalline olivine: grain boundary diffusion and the physical significance of the Andrade model for viscoelastic rheology. J. Geophys. Res. Solid Earth 103 (B11), 27267–27279. https://doi.org/10.1029/98JB02786.

Havlin, C., Holtzman, B.K., Hopper, E., 2021. Inference of thermodynamic state in the asthenosphere from anelastic properties, with applications to North American upper mantle. Phys. Earth Planet. Inter. 314 (March 2020), 106639 https://doi.org/10.1016/j.pepi.2020.106639.

Hiraga, T., Anderson, I., Zimmerman, M., Mei, S., Kohlstedt, D., 2002. Structure and chemistry of grain boundaries in deformed, olivine + basalt and partially molten lherzolite aggregates: evidence of melt-free grain boundaries. Contrib. Mineral. Petrol. 144 (2), 163–175. https://doi.org/10.1007/s00410-002-0394-1.

Hirth, G., Kohlstedt, D.L., 1995. Experimental constraints on the dynamics of the partially molten upper mantle: deformation in the diffusion creep regime. J. Geophys. Res. Solid Earth 100 (B2), 1981–2001. https://doi.org/10.1029/94JB02128.

Hirth, G., Kohlstedt, D.L., 1996. Water in the oceanic upper mantle: implications for rheology, melt extraction and the evolution of the lithosphere. Earth Planet. Sci. Lett. 144 (1–2), 93–108. https://doi.org/10.1016/0012-821X(96)00154-9.

Hirth, J.P., Wang, J., Hirth, G., 2019. A topological model for defects and interfaces in complex crystal structures. Am. Mineral. 104 (7), 966–972. https://doi.org/10.2138/am-2019-6892.

Hirth, John P., Hirth, G., Wang, J., 2020. Disclinations and disconnections in minerals and metals. Proc. Natl. Acad. Sci. 117 (1), 196–204. https://doi.org/10.1073/pnas.1915140117.

Holzheid, A., O’Neill, H.S.C., 1995. The Cr-Cr2O3 oxygen buffer and the free energy of formation of Cr2O3 from high-temperature electrochemical measurements. Geochim. Cosmochim. Acta 59 (3), 475–479. https://doi.org/10.1016/0016-7037(94)00287-V.

Hsu, S. En, Edwards, G.R., Sherby, O.D., 1983. Influence of texture on dislocation creep and grain boundary sliding in fine-grained cadmium. Acta Metall. 31 (5), 763–772. https://doi.org/10.1016/0001-6160(83)90092-5.

Isaak, D.G., 1992. High-temperature elasticity of iron-bearing olivines. J. Geophys. Res. 97, 1871–1885.

Jackson, I., 2000. Laboratory measurement of seismic wave dispersion and attenuation: recent progress. In: Karato, S.-I., Forte, A., Liebermann, R., Masters, G., Stixrude, L. (Eds.), Earth’s Deep Interior: Mineral Physics and Tomography from the Atomic to the Global Scale, 117. American Geophysical Union, pp. 265–289. https://doi.org/10.1029/GM117p0265. Geophysical Monograph Series.

Jackson, Ian, 2019. Viscoelastic behaviour from complementary forced-oscillation and microcreep tests. Minerals 9 (12). https://doi.org/10.3390/min9120721.

Jackson, I., Faul, U., 2010. Grainsize-sensitive viscoelastic relaxation in olivine: towards a robust laboratory-based model for seismological application. Phys. Earth Planet. Inter. 183 (1–2), 151–163. https://doi.org/10.1016/j.pepi.2010.09.005.

Jackson, I., Paterson, M.S., 1993. A high-pressure, high-temperature apparatus for studies of seismic wave dispersion and attenuation. Pure Appl. Geophys. 141 (2–4), 445–466. https://doi.org/10.1007/BF00998339.

Jackson, I., Paterson, M.S., Fitz Gerald, J.D., 1992. Seismic wave dispersion and attenuation in Åheim dunite: an experimental study. Geophys. J. Int. 108 (2), 517–534. https://doi.org/10.1111/j.1365-246X.1992.tb04633.x.

Jackson, I., Fitz Gerald, J.D., Kokkonen, H., 2000. High-temperature viscoelastic relaxation in iron and its implications for the shear modulus and attenuation of the Earth’s inner core. J. Geophys. Res. Solid Earth 105 (B10), 23605–23634. https://doi.org/10.1029/2000jb900131.

Jackson, I., Fitz Gerald, J.D., Faul, U.H., Tan, B.H., 2002. Grain-size-sensitive seismic wave attenuation in polycrystalline olivine. J. Geophys. Res. Solid Earth 107 (B12). https://doi.org/10.1029/2001JB001225. ECV 5-1-ECV 5-16.

Jackson, I., Faul, U.H., Fitz Gerald, J.D., Tan, B.H., 2004. Shear wave attenuation and dispersion in melt-bearing olivine polycrystals: 1. Specimen fabrication and mechanical testing. J. Geophys. Res. Solid Earth 109 (B6). https://doi.org/10.1029/2003JB002406.

Jackson, I., Barnhoorn, A., Aizawa, Y., Saint, C., 2009. Improved procedures for the laboratory study of high-temperature viscoelastic relaxation. Phys. Earth Planet. Inter. 172 (1–2), 104–115. https://doi.org/10.1016/j.pepi.2008.03.010.

Jackson, I., Faul, U.H., Skelton, R., 2014. Elastically accommodated grain-boundary sliding: new insights from experiment and modeling. Phys. Earth Planet. Inter. 228, 203–210. https://doi.org/10.1016/j.pepi.2013.11.014.

Kampfmann, W., Berckhemer, H., 1985. High temperature experiments on the elastic and anelastic behaviour of magmatic rocks. Phys. Earth Planet. Inter. 40 (3), 223–247. https://doi.org/10.1016/0031-9201(85)90132-3.

Karato, S.-I., 2008. Deformation of Earth MaterialsAn Introduction to the Rheology of Solid Earth. Cambridge University Press.

Karato, S.-I., 2012. On the origin of the asthenosphere. Earth Planet. Sci. Lett. 321–322, 95–103. https://doi.org/10.1016/j.epsl.2012.01.001.

Karato, S.-I., Spetzler, H.A., 1990. Defect microdynamics in minerals and solid-state mechanisms of seismic wave attenuation and velocity dispersion in the mantle. Rev. Geophys. 28 (4), 399–421. https://doi.org/10.1029/RG028i004p00399.

Karato, S.-I., Paterson, M.S., FitzGerald, J.D., 1986. Rheology of synthetic olivine aggregates: influence of grain size and water. J. Geophys. Res. 91 (B8), 8151. https://doi.org/10.1029/JB091iB08p08151.

Kê, T.-S., 1947. Experimental evidence of the viscous behavior of grain boundaries in metals. Phys. Rev. 71 (8), 533–546. https://doi.org/10.1103/PhysRev.71.533.

Lee, L.C., Morris, S.J.S., 2010. Anelasticity and grain boundary sliding. Proc. R. Soc. A: Math. Phys. Eng. Sci. 466 (2121), 2651–2671. https://doi.org/10.1098/rspa.2009.0624.

Lee, L.C., Morris, S.J.S., Wilkening, J., 2011. Stress concentrations, diffusionally accommodated grain boundary sliding and the viscoelasticity of polycrystals. Proc. R. Soc. A: Math. Phys. Eng. Sci. 467 (2130), 1624–1644. https://doi.org/10.1098/rspa.2010.0447.

Liu, C., Yoshino, T., Yamazaki, D., Tsujino, N., Gomi, H., Sakurai, M., et al., 2023. Effect of water on seismic attenuation of the upper mantle: the origin of the sharp lithosphere–asthenosphere boundary. Proc. Natl. Acad. Sci. 120 (32) https://doi.org/10.1073/pnas.2221770120.

Ma, Z., Dalton, C.A., Russell, J.B., Gaherty, J.B., Hirth, G., Forsyth, D.W., 2020. Shear attenuation and anelastic mechanisms in the Central Pacific upper mantle. Earth Planet. Sci. Lett. 536, 116148 https://doi.org/10.1016/j.epsl.2020.116148.

Marquardt, K., Faul, U.H., 2018. The Structure and Composition of Olivine Grain Boundaries: 40 Years of Studies, Status and Current Developments. Physics and Chemistry of Minerals, 45. Springer Berlin Heidelberg. https://doi.org/10.1007/s00269-017-0935-9.

McCarthy, C., Takei, Y., Hiraga, T., 2011. Experimental study of attenuation and dispersion over a broad frequency range: 2. The universal scaling of polycrystalline materials. J. Geophys. Res. Solid Earth 116 (9), 1–18. https://doi.org/10.1029/2011JB008384.

Morris, S.J.S., Jackson, I., 2009. Implications of the similarity principle relating creep and attenuation in finely grained solids. Mater. Sci. Eng. A 521–522, 124–127. https://doi.org/10.1016/j.msea.2008.09.157.

Muir, J.M.R., Jollands, M., Zhang, F., Walker, A.M., 2022. Controls on the distribution of hydrous defects in forsterite from a thermodynamic model. Phys. Chem. Miner. 49 (4), 7. https://doi.org/10.1007/s00269-022-01182-w.

Nakakoji, T., Hiraga, T., Nagao, H., Ito, S., Kano, M., 2018. Diffusion creep and grain growth in forsterite +20 vol% enstatite aggregates: 1. High-resolution experiments and their data analyses. J. Geophys. Res. Solid Earth 123 (11), 9486–9512. https://doi.org/10.1029/2018JB015818.

Nieh, T.G., Sherby, O.D., 2005. Superplasticity in Metals and Ceramics. Cambridge University Press.

Nitsan, U., 1974. Stability field of olivine with respect to oxidation and reduction. J. Geophys. Res. 79 (5), 706–711. https://doi.org/10.1029/JB079i005p00706.

Paterson, M.S., 1970. High-pressure, high-temperature apparatus for rock deformation. Int. J. Rock Mech. Min. Sci. 7 (5), 517–526.

Qu, T., Jackson, I., 2022. Dynamic modulus, internal friction, and transient creep at high temperature in austenitic stainless steel. Mater. Today Commun. https://doi.org/10.1016/j.mtcomm.2021.103073.

Qu, T., Jackson, I., Faul, U.H., 2021. Low-frequency seismic properties of olivine-orthopyroxene mixtures. J. Geophys. Res. Solid Earth 126 (10). https://doi.org/10.1029/2021JB022504.

Raj, R., Ashby, M.F., 1971. On grain boundary sliding and diffusional creep. Metall. Trans. A. 2 (4), 1113–1127. https://doi.org/10.1007/BF02664244.

Romanowicz, B.A., Mitchell, B.J., 2015. Deep Earth Structure: Q of the Earth from Crust to core. Treatise on Geophysics: Second Edition, 1. Elsevier B.V. https://doi.org/10.1016/B978-0-444-53802-4.00021-X.

Sasaki, Y., Takei, Y., McCarthy, C., Rudge, J.F., 2019. Experimental study of dislocation damping using a rock analogue. J. Geophys. Res. Solid Earth 124 (7), 6523–6541. https://doi.org/10.1029/2018JB016906.

Sherby, O.D., Wadsworth, J., 1989. Superplasticity-recent advances and future directions. Prog. Mater. Sci. 33 https://doi.org/10.1016/0079-6425(89)90004-2.

Sundberg, M., Cooper, R.F., 2008. Crystallographic preferred orientation produced by diffusional creep of harzburgite: effects of chemical interactions among phases during plastic flow. J. Geophys. Res. 113 (B12), B12208. https://doi.org/10.1029/2008JB005618.

Sundberg, M., Cooper, R.F., 2010. A composite viscoelastic model for incorporating grain boundary sliding and transient diffusion creep; correlating creep and attenuation responses for materials with a fine grain size. Philos. Mag. 90 (20), 2817–2840. https://doi.org/10.1080/14786431003746656.

Takei, Y., Karasawa, F., Yamauchi, H., 2014. Temperature, grain size, and chemical controls on polycrystal anelasticity over a broad frequency range extending into the seismic range. J. Geophys. Res. Solid Earth 119 (7), 5414–5443. https://doi.org/10.1002/2014JB011146.

Tan, B.H., Jackson, I., Fitz Gerald, J.D., 2001. High-temperature viscoelasticity of fine-grained polycrystalline olivine. Phys. Chem. Miner. 28 (9), 641–664. https://doi.org/10.1007/s002690100189.

Thom, C., Tielke, J.A., Marquardt, K., Mariani, E., Mecklenburgh, J., Wheeler, J., Hansen, L.N., 2020. Direct Measurement of Olivine Grain Boundary Viscosity. American Geophysical Union. Fall Meeting 2020, abstract #MR022-0016.

Vaughan, P.J., Kohlstedt, D.L., Waff, H.F., 1982. Distribution of the glass phase in hot-pressed, olivine-basalt aggregates: an electron microscopy study. Contrib. Mineral. Petrol. 81 (4), 253–261. https://doi.org/10.1007/BF00371679.

Wiens, D.A., Kelley, K.A., Plank, T., 2006. Mantle temperature variations beneath back-arc spreading centers inferred from seismology, petrology, and bathymetry. Earth Planet. Sci. Lett. 248 (1–2), 30–42. https://doi.org/10.1016/j.epsl.2006.04.011.

Xu, Y., Zimmerman, M.E., Kohlstedt, D.L., 2004. 10. Deformation behavior of partially molten mantle rocks. In: Rheology and Deformation of the Lithosphere at Continental Margins. Columbia University Press, pp. 284–310. https://doi.org/10.7312/karn12738-011.

Yabe, K., Sueyoshi, K., Hiraga, T., 2020. Grain-boundary diffusion creep of olivine: 1. Experiments at 1 atm. J. Geophys. Res. Solid Earth 125 (8), 1–33. https://doi.org/10.1029/2020JB019415.

Yamauchi, H., Takei, Y., 2016. Polycrystal anelasticity at near-solidus temperatures. J. Geophys. Res. Solid Earth 121 (11), 7790–7820. https://doi.org/10.1002/2016JB013316.

Zener, C.M., 1952. Elasticity and Anelasticity of Metals. University of Chicago Press.